ELSEVIER

Journal of Photochemistry and Photobiology A: Chemistry 111 (1997) 111–138

Journal of
PHOTOCHEMISTRY
AND
PHOTOBIOLOGY
A: CHEMISTRY

Theory of electron transfer reactions in photosynthetic bacteria reaction centers

Luís G. Arnaut, Sebastião J. Formosinho [1]

Chemistry Department, University of Coimbra, 3049 Coimbra Codex, Portugal

Accepted 20 July 1997

Abstract

The intersecting-state model and an electron tunneling model are used to calculate the rates of electron transfer (ET) reactions in *Rb. sphaeroides* reactions centers (RCs). The models characterize the reactants by their bond lengths, force constants and bond orders, and the RC by its refractive index and thermal expansion. The experimental distances and driving forces of the ET reactions are also employed in the calculations. The only extra kinetic parameter required by the models is the coupling between reactive and non-reactive modes, which is assumed to be constant and is taken from earlier studies on similar intramolecular ETs. No additional parameters are fitted in the calculation of ETs from the excited special pair to an accessory bacteriochlorophyll (B_L), from B_L to bacteriopheophytin (H_L), from $H_L^{\bullet}$ to the primary quinone acceptor (Q_A), from $Q_A^{\bullet}$ to the secondary quinone acceptor (Q_B), and in the charge recombinations between each of the reduced cofactors and the photo-oxidized special pair ($P^{\bullet +}$); the reduction of $P^{\bullet +}$ by a cytochrome c in *Rb. sphaeroides* and in *Chromatium* is also studied. The calculated free-energy and temperature dependences are within one order of magnitude of the rates measured in mutant and cofactor-substituted RCs, except for the temperature dependence of the charge shift from $Q_A^{\bullet}$ to Q_B. It is suggested that the rate measured for this process does not reflect an elementary ET reaction.

Keywords: Electron-transfer; Intersecting-state model; Photosynthesis; Reaction center

1. Introduction

The study of photosynthesis is, and probably always will be, the greatest odyssey of the photochemist [1]. In photosynthesis, light energy is absorbed by antenna molecules and efficiently transferred to a chlorophyll–protein complex called the photosynthetic reaction center (RC). Here, the conversion of light energy into chemical energy occurs by a cascade of photoinduced electron-transfer (ET) processes. This process is of critical importance for the global energy balance and has been the focus of many research projects over the last few decades. A major breakthrough in the understanding of photosynthesis was the determination to atomic resolution of the three-dimensional structure of the RC from two species of purple non-sulphur bacteria, *Rhodopseudomonas (Rps.) viridis* [2,3] and *Rhodobacter (Rb.) sphaeroides* [4,5]. The photosynthetic RC is now one of the best characterized organized ET systems. The variety of different ET reactions in RCs, ranging in timescales from picoseconds to seconds, and the detail in which their distance, free-energy and temperature dependencies are known, has rendered it a model system to study ET processes in proteins [6]. The availability of mutagenesis protocols for *Rb. sphaeroides* and the ability of these organisms to grow nonphotosynthetically while still expressing RC, lead to the production of many RC mutants of this bacteria. The wealth of information concerning perturbations in these RCs, in particular mutations, changes in cofactors, temperature and pH, has stimulated us to assess the applicability of ET theories to calculate the distance, free-energy and temperature dependences of the rates of all types of ET reactions taking place in the native and perturbed *Rb. sphaeroides* RCs. The similar architecture of *Rb. sphaeroides* and *Rps. viridis* RCs [7] and the refinement of the structure of the later to a resolution of 2.3 Å [8], has also prompted us to use the precisely measured distances between cofactors of *Rps. viridis* RC as models for the edge-to-edge distances (r_e) between cofactors in *Rb. sphaeroides*. Deisenhofer, Michel et al. [8] define r_e as the distance between the carbon atom at the edge of the π-system of the donor in closest contact with that of the acceptor.

The RCs isolated from wild-type strains of *Rb. sphaeroides* RC consist of three protein subunits and ten cofactors. The protein subunits are called (H), (L) and (M). The cofactors

---

[1] Also at: Escola Superior de Ciências e Tecnologia, Universidade Católica Portuguesa, 3500 Viseu, Portugal.

1010-6030/97/$17.00 © 1997 Elsevier Science S.A. All rights reserved
PII S1010-6030(97)00225-6

are four type *a* bacteriochlorophylls, two type *a* bacteriopheophytins, two ubiquinones, a ferrous non-heme iron ion and a carotenoid. The RC crystal structure shows that the (H) subunit does not come into close contact with the redox active cofactors. The (L) and (M) chains are transmembrane proteins with homologous structures and have about one-third of their amino acids in common [9], even though their overall three-dimensional structures are quite similar and related to each other in the RC by a local two-fold symmetry axis (Fig. 1). The non-protein cofactors are embedded in the (L) and (M) chains. Two bacteriochlorophylls form the so-called 'special pair', P, with the centers separated by 3.1 Å. This pair is flanked by two symmetrically placed monomeric 'accessory' bacteriochlorophylls (B_L and B_M), at an edge-to edge distance r_e = 4.7 Å. 3.8 Å from the edge of each of these accessory bacteriochlorophylls is the edge of a bacteriopheophytin (H_L and H_M). The primary ubiquinone-10 (Q_A) is found r_e = 9.0 Å from H_L and 13.5 Å from the second ubiquinone-10 (Q_B). The isoprenoid side chain of Q_A is close to H_L. The iron ion lies approximately on the two-fold symmetry axis relating the cofactors of the (L) and (M) sides, and between the two quinones. The carotenoid is within 4 Å of H_M in the wild type, and there is no corresponding carotenoid on the (L) side.

The electronic excitation of the *Rh. sphaeroides* special pair leads to a cascade of ET reactions, $P^* \rightarrow [P^{+} B_L^{-}] \rightarrow [P^{\bullet +} H_L^{\bullet -}] \rightarrow [P^{\bullet +} Q_A^{\bullet -}] \rightarrow [P^{\bullet +} Q_B^{\bullet -}]$, which produce the charge-separated state $[P^{\bullet +} Q_B^{\bullet -}]$ across the bacterial membrane, with almost unit efficiency even at cryogenic temperatures. $Q_B^{\bullet -}$ needs to picks up a second electron and two protons before it dissociates from the RC in the form of Q_BH_2. The protons and electrons on Q_BH_2 are then transferred back through the membrane by the cytochrome b/c_1 complex. The proton gradient generated across the membrane is used to synthesize adenosine triphosphate. The cytochrome b/c_1 complex reduces an exogenous ferricytochrome c_2, which then associates with the RC and reduces $P^{\bullet +}$. Meanwhile, the Q_B site is re-filled from a pool of quinones in the membrane and a new ET sequence may be started.

In principle, a comprehensive theory of ET rates in wild-type and mutant RCs of *Rb. sphaeroides* should calculate the rates of all the types of charge-separation reactions indicated above and of the appropriate charge-recombination reactions, using only (structural, thermodynamic, spectroscopic and electronic) information on the reactants and products of each step. This is a very complex task, which has been partially fulfilled by Kuhn and Kitzing [10,11]. The alternative has been a phenomenological analysis based on a first-order time-dependent perturbation theory [12–14], where several physical parameters are invoked to rescue the situation and fit the experimental distance, free-energy and temperature dependences of the rates.

The objective of our work is to show that a detailed treatment of these ET rates can be done within the framework of the intersecting-state model [15,16]. This model describes the reactants and products in terms of their effective bond lengths, force constants and bond orders, using spectroscopic and structural data previously employed in self-exchange reactions [17–19]. The rates of highly exothermic reactions have a free-energy dependence that is modulated by the coupling between reactive and non-reactive modes. The narrow range of the parameter Λ which describes this coupling was obtained in a detailed study of intramolecular ET in solution [20]. Thus, we calculate the rates of the charge-separation and charge-recombination reactions taking place in wild-type

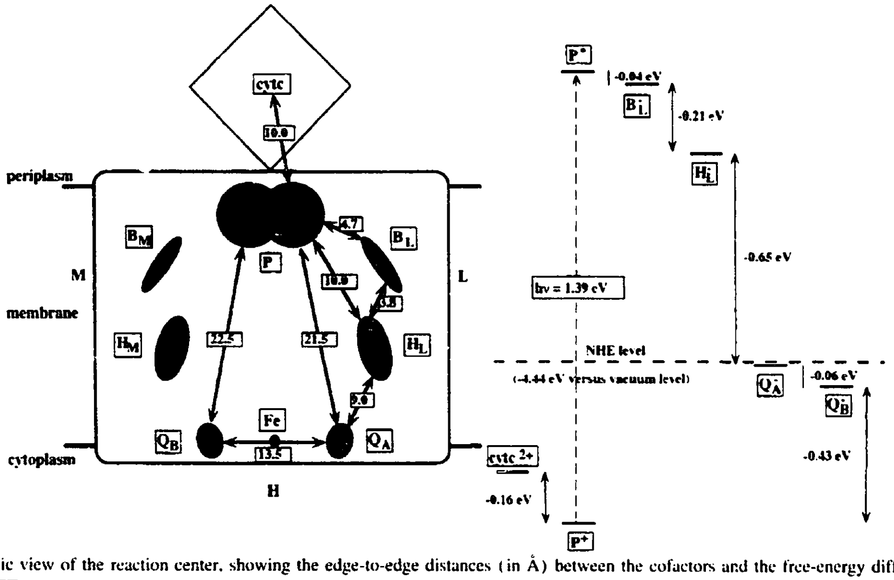

Fig. 1. Schematic view of the reaction center, showing the edge-to-edge distances (in Å) between the cofactors and the free-energy differences (in eV) involved in the ET steps.

and mutant RCs of *Rb. sphaeroides* in the 4–310 K temperature range, using only reaction free-energies, physical parameters of the reactants and protein medium, and a coupling constant. Our calculations do not require a detailed knowledge of the protein structure nor the adjustment of parameters. The following remarkable features exhibited by RCs are addressed:

(i) The forward ET rates are much faster than the charge-recombination rates, leading in 150 μs to a separation of charges with high efficiency over a distance of 30 Å.

(ii) The rates of the $H_L^{\bullet -} \rightarrow Q_A$ and $Q_A^{\bullet -} \rightarrow P^{\bullet +}$ steps are only mildly dependent on variations of their free energies, giving rise to rather flat free-energy profiles over a range of 0.3 eV. However, the rates of the $P^* \rightarrow B_L$, $Q_B^{\bullet -} \rightarrow P^{\bullet +}$ and $\mathrm{cytc}^{2+} \rightarrow P^{\bullet +}$ steps increase by a factor of 10 at room temperature when their driving forces increase by 0.15 eV.

(iii) The rates of the $P^* \rightarrow B_L$, $H_L^{\bullet -} \rightarrow Q_A$ and $Q_A^{\bullet -} \rightarrow P^{\bullet +}$ steps increase slightly when the RCs are cooled from room temperature to cryogenic temperatures. However, for temperatures above 250 K, the rates of the $Q_A^{\bullet -} \rightarrow Q_B$, $Q_B^{\bullet -} \rightarrow P^{\bullet +}$ and $\mathrm{cytc}^{2+} \rightarrow P^{\bullet +}$ reactions show an Arrhenius behavior. The change from a high-temperature activated region to a temperature-independent rate at low temperatures exhibited by the photosynthetic bacterium *Chromatium vinosum* [21] comes naturally in our calculations.

(iv) ET proceeds predominantly via the L-branch of the RC.

2. Overview

2.1. Experimental information

The two bacteriochlorophyll molecules of the special pair are nearly parallel, separated by 3.1 Å, and are offset so that there is an overlap of only one pyrrole ring of each molecule. There is some debate on whether histidines (L)173 and (M)202 are true ligands of the magnesium ions of the special pair. The Mg–N distances reported for histidine (M)202 (2.2–2.7 Å), and for histidine (L)173 (2.6–3.2 Å), are longer than the Mg–N distances observed for small-molecule structures of chlorophyll derivatives with five-coordinate magnesium (2.0–2.1 Å) [22]. When these histidine ligands of the special pair are replaced by a bulky, non-coordinating ligand such as leucine or phenylalanine, the special pair assembles but the bacteriochlorophyll whose axial histidine was replaced loses its Mg atom. It was recently shown that the nature of the axial ligand has little influence on the properties of the special pair [23]. Wild-type RCs show fully reversible Nernstian behavior with an electrochemical midpoint for the special pair of $E_m \approx 0.500$ V versus the normal hydrogen electrode, NHE [24,25].

The charge separation in the RC is triggered by the electronic excitation of the special pair, P*, which has an excited state energy $E_S = 1.39$ eV [26]. The ET time of P* in the isolated RC is approximately 3.5 ps at room temperature [27–30]; measured from a single exponential fit to the stimulated emission of P* in the infrared, this decreases to 1.2 ps at 8 K [27]. There is general agreement that the reduced form of H_L is generated with the photoinduced ET from the special pair, but the mechanism of this forward, selective, charge-separating step is not settled. Despite the structural symmetry of the RC, the reaction proceeds preferentially along the L-branch [31]. A selectivity larger than five favouring the L-branch relative to the M-branch was obtained at room temperature for RCs of *Rps. viridis* and *Rb. sphaeroides* [32]. The lower limit of this selectivity increases to 25 at 80 K for *Rb. sphaeroides* RCs [33], and to 200 for *Rps. viridis* RCs at 90 K [34]. The most controversial issue has been the role played by the accessory bacteriochlorophylls. The difficulty in observing a reduced accessory bacteriochlorophyll (B_L^{-}) and the 10.0 Å long edge-to-edge distance between P* and H_L, lead to the proposal of three possible mechanisms for this primary charge separation: (i) the energy of B_L^{-} is much higher than that of P* [35], and B_L acts as a superexchange mediator between P* and H_L [33,36,37]; (ii) the energy of B_L^{-} is similar to that of P* and the electron exchange between them is reversible [38]; (iii) the energy of B_L^{-} is sufficiently lower than that of P* [39], so that B_L^{-} is a real kinetic intermediate, with a time constant for its formation that is longer than the time constant for its ET to H_L [40]. The view currently emerging is that the energy of B_L^{-} is approximately 0.04 eV lower than that of P* [38,41]. Thus, we will approach the mechanism for the initial charge separation as the transfer of an electron from P* to B_L and then from B_L^{-} to H_L.

The free-energy difference between P* and $H_L^{\bullet -}$ has been measured by different techniques. A free-energy gap of 0.14 eV was obtained from the delayed fluorescence at room temperature, decreasing to 0.05 eV at 100 K and to 0.01 eV at 20 K [42,43]. A gap of 0.263 eV was obtained from the energies of P* and ^{3}P, associated with magnetic field effect studies on the free-energy difference between ^{3}P and $^3[P^{\bullet +} H_L^{\bullet -}]$, and this gap was found to be approximately independent of temperature [44]. A gap of 0.20 to 0.25 eV has been determined by MARY spectroscopy [45]. The discrepancy between these two types of measurements has been assigned to their different time scales: the delayed fluorescence measurements are made with a nanosecond time window involving an unrelaxed $[P^{\bullet +} H_L^{\bullet -}]$ ion pair [46]. It is now accepted that the relaxed $[P^{\bullet +} H_L^{\bullet -}]$ state lies 0.25–0.28 eV below the P* state in wild-type RC [24]. The free-energy differences for the ET from P* to B_L ($\Delta G^0 \approx -0.04$ eV) and from B_L^{-} to H_L ($\Delta G^0 \approx -0.21$ eV), together with femtosecond transient absorption studies [38], favour the sequential mechanism. Within the framework of this mechanism, the rate constants for each of the two steps are approximately the inverse of the corresponding lifetimes. Lifetimes of 3.5 and 0.9 ps were obtained by Zinth and coworkers [40,47], and of 3.1 and 1.5 ps were obtained by Holzwarth and Müller [38]. Replacing $\mathrm{H_L}$ by pheophytins decreases the driving force of the ET from $\mathrm{B_L^{-}}$ to $\mathrm{H_L}$, and lifetimes of 1.5 ps were measured for $\mathrm{B_L^{-}}$ [41,48].

ET from $\mathrm{H_L^{\bullet -}}$ to $\mathrm{Q_A}$, in the native and in $\mathrm{Q_A}$-site reconstituted RC, has been studied in great detail [49,50]. Based on the electrochemical midpoint potentials of $\mathrm{H/H^{\bullet -}}$ ($E_m = -0.70$ V versus NHE) and of the native ubiquinone-10 $\mathrm{Q_A}$ cofactor ($E_m = -0.05$ V), Dutton and Gunner estimated that ΔG^0 for the ET from $\mathrm{H_L^{\bullet -}}$ to the native $\mathrm{Q_A}$ is -0.65 eV [50]. These authors also presented arguments for a relatively temperature independent value of ΔG^0. Using the electrochemical midpoint potential of $\mathrm{P^{+}/P}$ ($E_m = 0.50$ V), they also estimated that charge recombination from the native $\mathrm{Q_A^{\bullet -}}$ to $\mathrm{P^{+}}$ has $\Delta G^0 \approx -0.50$ eV, which argues in favour of $\Delta G^0 \approx -0.24$ eV for the free-energy difference between P^* and $[\mathrm{P^{\bullet +}\ H_L^{\bullet -}}]$. By using a wide range of quinone and non-quinone molecules in the $\mathrm{Q_A}$ site, Dutton and Gunner extensively probed the free-energy dependence of the $\mathrm{H_L^{\bullet -}}$ to $\mathrm{Q_A}$ ET rate. Their results show that these rates depend only weakly on ΔG^0 over a 0.3 eV range, covering the values observed in the native system. The lifetime of $\mathrm{H_L^{\bullet -}}$ in the wild type RC, 148 ps [38], seems to be shorter than the lifetimes of $\mathrm{Q_A}$-site reconstituted RCs [51]. Furthermore, the rates appear to decrease slightly from room temperature to 113 K and then increase as the temperature continues to decrease to 14 K [50].

The free-energy gap between the $[\mathrm{P^{\bullet +}\ Q_A^{\bullet -}}]$ and $[\mathrm{P^{\bullet +}\ Q_B^{\bullet -}}]$ states has been measured by many techniques and all the methods give remarkably consistent values of -0.06 to -0.08 eV [52,53]. At 294 K the ET time for transfer from $\mathrm{Q_A^{\bullet -}}$ to $\mathrm{Q_B}$ in native RCs is 150 μs [54]. The lifetime increases to 350 μs when the RCs are depleted of the non-heme iron, but recovers the original value when the RCs are reconstituted with divalent metal ions [54]. A Van't Hoff plot of the equilibrium constants of the $[\mathrm{P^{\bullet +}\ Q_A^{\bullet -}}] \rightarrow [\mathrm{P^{\bullet +}\ Q_B^{\bullet -}}]$ reaction at temperatures ranging from 273 to 303 K, reveals that the equilibrium constant increases with a decrease in temperature [52]. The temperature dependence of the ET rate was also measured over that temperature range and linear Arrhenius and Eyring plots were obtained [52]. The Arrhenius plot gave $A = 2 \times 10^{14}$ $\mathrm{s^{-1}}$ and $E_a = 60$ kJ $\mathrm{mol^{-1}}$. The Eyring plot gave an activation enthalpy of 57 kJ $\mathrm{mol^{-1}}$ and a near zero activation entropy. The large pre-exponential factor (or the near zero activation entropy) is not consistent with a first-order ET between donor and acceptor separated by 13.5 Å. The temperature dependences of intramolecular ETs across rigid spacers keeping electron donor and acceptor about 10 Å apart [55–57], have pre-exponential factors in the 10^8–10^{10} $\mathrm{s^{-1}}$ range. Furthermore, the activation energy obtained by Mancino et al. [52] is much higher than the $E_a \approx 20$ kJ $\mathrm{mol^{-1}}$ obtained in the temperature dependence studies of electron self-exchanges of organic species in solution [58]. $E_a \approx 20$ kJ $\mathrm{mol^{-1}}$ is also the value that fits the temperature dependence of the intramolecular ET from the biphenylyl to naphthyl group across a steroid spacer [55], which has a driving force similar to that of the $\mathrm{Q_A^{\bullet -} \rightarrow Q_B}$ step. Given the complex pH behavior of the $\mathrm{Q_A^{\bullet -} \rightarrow Q_B}$ step [52], it is possible that the observed temperature dependence is not that of the ET reaction.

While an electron is transferred from $\mathrm{Q_A^{\bullet -}}$ to $\mathrm{Q_B}$, an exogenous cytochrome c_2, $\mathrm{cytc^{2+}}$, reduces the photo-oxidized primary donor, $\mathrm{P^{\bullet +}}$, with a characteristic lifetime of ET of 960 ns [59]. This water-soluble single heme cytochrome c_2, whose three-dimensional structure has been determined [60], does not crystallize as an integral part of the RC. In this respect *Rb. sphaeroides* differs from *Rps. viridis*, which has a tetra-heme c-type cytochrome tightly bound to the membrane polypeptide core of the RC. Thus, it was possible to measure $r_e \approx 11$ Å between the special pair and the closest heme of the bound cytochrome in *Rps. viridis* and a transfer time of 270 ns [61]. For the analogous distance in *Rb. sphaeroides* values between 9 and 14 Å have been proposed [59]. More recently, the RC and $\mathrm{cytc^{2+}}$ from *Rb. sphaeroides* were co-crystallized [62]. The data were not of good enough quality to unambiguously position the $\mathrm{cytc^{2+}}$ and its manual positioning into the electron density patches lead to $r_e \approx 14$ Å. From the midpoint potentials of $\mathrm{cytc^{2+}/cytc^{3+}}$ and $\mathrm{P/P^{\bullet +}}$ pairs, $\Delta G^0 \approx -0.16$ eV was estimated for the wild type RC [59]. Measurements of ET rates from $\mathrm{cytc^{2+}}$ to a series of mutant RCs showed that these rates are strongly dependent of their driving force [59]. A temperature dependence study revealed that these rates follow a linear Arrhenius plot over the temperature range 240–300 K, with an activation energy ca. 20 kJ $\mathrm{mol^{-1}}$ [63]. This is higher than the activation energy measured in the same temperature range for *Chromatium* ($E_a = 13.8$ kJ $\mathrm{mol^{-1}}$, $\Delta G^0 \approx -0.186$ eV) and *Rps. viridis* ($E_a = 6.7$–8.8 kJ $\mathrm{mol^{-1}}$, $\Delta G^0 \approx -0.12$ eV) [64]. Apparently, E_a decreases with an increase in the tightness of the association between the cytochrome and the RC [63].

An extraordinary feature of the structure of the RC is that the distances for the forward, charge-separating steps are always shorter than those of the competing back, charge-recombination steps. The energies of the charge-recombination steps can be obtained from the excited state energy of the special pair and the energies of the charge-separating steps mentioned above. A limit of 10 to 20 ns for the charge-recombination time between $\mathrm{H_L^{\bullet -}}$ and $\mathrm{P^{\bullet +}}$ in wild RCs can be estimated from the near unity efficiency of its charge separation and from the ET time from $\mathrm{H_L^{\bullet -}}$ to $\mathrm{Q_A}$ [43 65]. This limit is unlikely to change appreciably with the temperature because neither the efficiency nor the charge-separation rate are significantly temperature dependent. Actually, a small decrease in the recombination rate was estimated by Ogrodnik et al., from 5.5×10^7 $\mathrm{s^{-1}}$ at 290 K to 1.5×10^7 $\mathrm{s^{-1}}$ at 90 K [66]. Charge-recombination lifetimes ranging from 6 to 14 ns were measured in wild-type RCs with non-native quinones in the $\mathrm{Q_A}$ site [51].

Charge recombination between various semiquinones in the $\mathrm{Q_A^{\bullet -}}$ site and $\mathrm{P^{\bullet +}}$ were studied both as a function of the temperature and of the free-energy gap [67]. Although Dutton and Gunner investigated a range of ΔG^0 values extending from −0.11 to −0.94 eV, they found only a small dependence of the ET rates on their driving forces. These ET rates were found to be virtually independent of the temperature from 5 to 100 K, and to decrease several-fold from 100 to 300 K. Furthermore, this significant decrease in rate with increasing temperature is observed in a range of ΔG^0 from −0.4 to −0.6 eV. At each temperature, there is an increase in the rate of $P^{\bullet +}$ reduction with the increase in the tail length of the quinone in the $Q_A^{\bullet -}$ site. The edge-to-edge distance between $Q_A^{\bullet -}$ and $P^{\bullet +}$ was not reported by Deisenhofer et al. [8]. Moser et al. estimated this distance to be 22.5 Å [6]. The criterion used by Moser et al. gives systematically larger r_e values than that of Deisenhofer et al. To maintain the internal consistency of our calculations, we must correct for the differences between these two sources and use $r_e \approx 21.5$ Å for the $Q_A^{\bullet -}$ to $P^{\bullet +}$ charge recombinations.

In native RCs, the charge-recombination between the secondary semiquinone, $Q_B^{\bullet -}$, and the oxidized special pair, $P^{\bullet +}$, proceeds via an indirect path involving the intermediate state $[P^{\bullet +}\ Q_A^{\bullet -}\ Q_B]$ [68]. However, the direct charge recombination between the native semiquinone in the Q_B site and $P^{\bullet +}$ can be measured by raising the energy of the $[P^{\bullet +}\ Q_A^{\bullet -}\ Q_B]$ state through substitution of the native quinone in the Q_A site by low potential quinones [69]. The observed direct charge-recombination rates increase from 0.115 s^{-1} at 277 K to 0.176 s^{-1} at 313 K. Feher and coworkers studied the free-energy dependence of these rates by making use of their pH dependence [53,69]. For the reasons discussed above, we correct the edge-to-edge distance given Moser et al., $r_e \approx 23.5$ Å [6] by the difference with the data of Deisenhofer et al. [8]. Thus, we have $r_e \approx 22.5$ Å for this charge recombination.

Fig. 1 summarizes the experimental structural and energetic data on the nine types of ET reactions experimentally measured in native *Rb. sphaeroides* RCs.

2.2. *Conventional non-adiabatic multiphonon theory*

Most of the attempts to model ET processes in biological systems have been based on the non-adiabatic multiphonon radiationless transition theory [70,71]. According to this model, the theoretical free-energy gap dependence is given by [72]

$$k_{\mathrm{NMT}} = \left(\frac{2\pi}{\hbar}\right)|V^2|F(\lambda_m, \hbar\omega_m, \lambda_i, \hbar\omega_i, \Delta G^0, T) \tag{1}$$

where V is the electronic coupling between donor and acceptor and F is the nuclear Franck–Condon factor. This factor is characterized by low-frequency (medium) vibrational modes with an average frequency ω_m and a reorganization energy λ_m, and by the effective high-frequency (intramolecular) vibrational mode ω_i with a reorganization energy λ_i. This factor has contributions from the medium modes (F_m) and from the intramolecular high-frequency modes (F_i) [72]

$$\begin{aligned} &F(\lambda_m, \hbar\omega_m, \lambda_i, \hbar\omega_i, \Delta G^0, T) \\ &\quad = \sum_{n=0}^{\infty} F_m(\Delta G^0 - n\hbar\omega_i)F_i(n) \end{aligned} \tag{2}$$

which can be written

$$\begin{aligned} F_m(\Delta E) = (\hbar\omega_m)^{-1}\left(\frac{\bar{\upsilon}+1}{\bar{\upsilon}}\right)^{p/2} \\ \times \exp[-S_m(2\bar{\upsilon}+1)]I_p\{2S_m[\bar{\upsilon}(\bar{\upsilon}+1)]\}^{1/2} \end{aligned} \tag{3}$$

$$F_i(n) = \frac{\exp(-S_i)S_i^n}{n!} \tag{4}$$

where

$$\bar{\upsilon} = \left[\exp\left(\frac{\hbar\omega_m}{k_B T}\right) - 1\right]^{-1} \tag{5}$$

is the mean thermal vibrational excitation,

$$S = \frac{\lambda}{\hbar\omega} \tag{6}$$

is the vibrational-electron coupling,

$$p = \frac{\Delta G}{\hbar\omega_m} \tag{7}$$

and $I_p(\cdots)$ is the modified Bessel function of order p. The ΔG^0 and T dependencies of the several ET processes in *Rb. sphaeroides* RCs have been experimentally explored over a wide range of values, but five theoretical parameters are needed to describe such dependences and have to be fitted to the experimental data. In principle, the electronic coupling V can be calculated either as the electron tunneling probability through an uniform effective barrier [6] or from a superexchange model accounting for the nature of the bridge [73]. A different sort of algorithm constructs ET pathways from covalent linkages between adjacent atoms, hydrogen bonds, and through space jumps [74]. The search for the optimal pathways that connect donor and acceptor is based on a crystal structure. A serious problem with the application of this method to calculate ET distance dependencies in RCs, is that the density of the published structure of *Rb. sphaeroides* appears to be 10% less than that expected from typical values of protein specific gravity [75]. The unresolved atoms, presumably water molecules, may be of critical importance to the ET pathways. Given these difficulties, the practice is to fit V to reproduce the value of the maximum rate constant observed for a given system. It should be emphasized that the validity of this non-adiabatic theory rests on the assumption that the electronic coupling is weak relative to the characteristic vibrational energies of the system [76]. For ET in a polar liquid, the medium reorganization energy λ_m can be expressed in terms of the Marcus–Levich expression [77–80], developed for changes in the charging energy in rigid conductors in a dielectric continuum [81], but for biological systems λ_m is obtained from the ΔG^0 value corresponding to maximum rate. The intermolecular protein modes have frequencies in the range $\hbar\omega_m = 0–150\ \mathrm{cm^{-1}}$ [82], and $\hbar\omega_m$ is fitted to reproduce the curvature of the free-energy dependence. The high-frequency modes correspond either to metal–ligand vibrations in the first coordination shell of solvated ions ($\hbar\omega_i \approx 300–500\ \mathrm{cm^{-1}}$), or to the C–C ($\hbar\omega_i \approx 1000–1600\ \mathrm{cm^{-1}}$) and C–H ($\hbar\omega_i \approx 3000\ \mathrm{cm^{-1}}$) stretching modes of organic molecules [83]. The asymmetry of the free-energy plots determines the choice of $\hbar\omega_i$, because larger values of $\hbar\omega_i$ give a slower decrease in the rates with an increase in the driving force of the ETs in the inverted region [83]. The reorganization energy of the high-frequency modes is related to the horizontal displacement of their (oxidized and reduced) potential energy surfaces [84,85]; the practice in biological systems is to obtain its value from the temperature dependence of the ET rates in the inverted region. With $\lambda_i = 0$ the rates in the inverted region are strongly dependent on the temperature; however, for the protein medium of the RC, $\lambda_i = 0.186$ eV leads to nearly temperature independent rates in this region [86].

The gross features of the temperature dependence of the decay of P* are reproduced by the non-adiabatic ET theory in the limit of activationless rates using $\hbar\omega_m = 80–100\ \mathrm{cm^{-1}}$ and presuming that the driving force of the reaction is that of the process $[\mathrm{P^{*}H_L}] \to [\mathrm{P^{+}H_L^{\bullet-}}]$, i.e. $\lambda = \Delta G^0 = -0.25$ eV [87]. Alternatively, incorporating high-frequency quantum modes, $\hbar\omega = 1500\ \mathrm{cm^{-1}}$ and $\lambda_i > 0.1$, practically activationless ET is expected to prevail over the range $0.5 \leq -\Delta G^0/\lambda \leq 10$ [86], and the temperature dependence of the decay of P* can be fitted within the sequential model. These parameters were also used together with $V = 2.5$ meV, $\lambda = 0.10$ eV and $\hbar\omega_m = 95\ \mathrm{cm^{-1}}$ to reproduce the free-energy dependence of the primary charge separation using the sequential model. The complete set of parameters adjusted in these calculations [72] is shown in Table 1.

The rate of charge recombination between $\mathrm{H_L^{\bullet}}$ and $\mathrm{P^{\bullet+}}$ decreases by a factor of 3.8 when the temperature is decreased from 290 to 90 K [66]. This feature can be reproduced with $\lambda_i \approx 0.1–0.2$ eV, $\hbar\omega_i = 1500\ \mathrm{cm^{-1}}$ and $\lambda_m \approx 0.2$ eV [86], under the assumption V is nearly the same as for the charge-recombination reaction in the triplet state, $V = 0.1$ meV [89].

The ET rates from $\mathrm{H_L^{\bullet-}}$ to $\mathrm{Q_A}$ and from $\mathrm{Q_A^{\bullet-}}$ to $\mathrm{P^{\bullet+}}$ are independent of the temperature over a large range of $-\Delta G^0$, showing that ET in RCs is coupled to intermediate (medium) and high-energy (internal) vibrations [50]. With the parameters shown in Table 1 it is possible to model the general features of the dependence of the ET rate on $-\Delta G^0$ and temperature. However, this theory cannot accommodate the slower rate from $\mathrm{H_L^{\bullet-}}$ to $\mathrm{Q_A}$ at 113 K compared with values 295, 35 or 14 K [50]. This can only be explained assuming that the value of V depends on the temperature. Such a dependence was attributed to temperature-dependent changes in the protein structure [50]. The decrease in rates with increase in temperature observed in the $\mathrm{Q_A^{\bullet-}}$ to $\mathrm{P^{\bullet+}}$ charge recombinations over a range of $-\Delta G^0$ from 0.4 to 0.6 eV, also supports an expansion or reorientation of the RC with increase in temperature [67]. The analysis of this system using the non-adiabatic ET theory requires that higher energy molecular vibrations play a dominant role in the ET process. One set of parameters used to fit the experimental rates is shown in Table 1.

The temperature dependence of the reduction of $\mathrm{P^{\bullet+}}$ by cytochrome c_2 in *Rb. sphaeroides* was studied in the 230–300 K range. An Arrhenius behavior with an activation energy between 20–24 kJ mol^{-1} was observed for the first-order cytc-RC complex electron donation: the rate constant decreases from $1.7 \times 10^6\ \mathrm{s^{-1}}$ at 295 K to $1.6 \times 10^5\ \mathrm{s^{-1}}$ at 238 K [63]. Below this temperature it was not possible to analyse the kinetics of the first-order reduction of $\mathrm{P^{\bullet+}}$. A more favourable situation occurs in bacteria where the cytochrome is more firmly bound to the RC, as in *Rps. viridis* and *Chromatium*. Activation energies lying between 6.7 and 8.8 kJ mol^{-1} have been measured over the same temperature range for ET from the highest potential heme to $\mathrm{P^{\bullet+}}$ in *Rps. viridis* RC [64]. The high-temperature region of cytochrome c oxidation in *Cromatium* has an activation energy of 13.8 kJ mol^{-1} [21,90]. The most interesting feature of this system is that the ET rate drops from about $10^6\ \mathrm{s^{-1}}$ at 300 K to $3 \times 10^2\ \mathrm{s^{-1}}$ at 100 K and then remains essentially constant down to 4 K [21,91,92]. The reasons for this sudden change in behavior around 120 K are still a matter of debate. Initially it was proposed that the sharp break in the experimental data was due to the onset of nuclear tunneling at low temperatures, and the data were fitted with a very large coupling $V \approx 90\ \mathrm{cm^{-1}}$, a (presumably intramolecular) vibrational frequency of $\hbar\omega = 500\ \mathrm{cm^{-1}}$ and a huge intramolecular reorganization energy $\lambda_i = 2.29$ eV [85]. This set of parameters is not con-

Table 1
Parameters fitted to the kinetic data in the description of ET rates in RCs, using the multiphonon non-adiabatic theory

System	V (meV)	$\hbar\omega_m$ (cm^{-1})	λ_m (meV)	$\hbar\omega_i$ (cm^{-1})	λ_i (meV)	S_i	Fitting	Refs.
$[\mathrm{P^{*}B_L}] \to [\mathrm{P^{+}B_L^{-}}]$	2.5	95	100	1500		0.5	$\Delta G, T$	[72]
$[\mathrm{P^{+}H_L^{\bullet-}}] \to [\mathrm{P H_L}]$	0.11		200	1500		0.5–1	T	[86]
$[\mathrm{H_L^{\bullet-} Q_A}] \to [\mathrm{H_L Q_A^{\bullet-}}]$	$(22–8.7) \times 10^{-2}$	120	600	1600	200		$\Delta G, T$	[50]
$[\mathrm{Q_A^{\bullet-} P^{+}}] \to [\mathrm{Q_A P}]$	$(26–8.8) \times 10^{-6}$	120	375	1600	200		$\Delta G, T$	[50]
$[\mathrm{cytc^{2+} P^{+}}] \to [\mathrm{cytc^{3+} P}]$	1.2×10^{-4}	100	124	1000	62		T[a]	[88]

[a] The fitting of three additional parameters was also required to reproduce the temperature dependence of *Cromatium*; these parameters were assigned to "protein specific dynamics".

sistent with the parameters shown in Table 1 for similar reactions, and an alternative mechanism postulating two parallel oxidations involving two different heme groups in the cytochrome c protein, was proposed by Bixon and Jortner [93]. In the low-temperature limit an activationless process dominates ($\lambda = -\Delta G^0 = 0.432$ eV) and the rate is fitted with $V \approx 8 \times 10^{-4}$ cm^{-1} and $\hbar\omega = 100$ cm^{-1}, whereas the high-temperature limit of the rate is described by the high-temperature classical limit of the non-adiabatic ET theory [70,76,94]

$$k_{\mathrm{HT}} = \frac{2\pi}{\hbar} |V|^2 \frac{1}{\sqrt{4\pi\lambda RT}} \exp\left[-\frac{(\Delta G^0 + \lambda)^2}{4\lambda RT} \right] \tag{8}$$

using the same value of ΔG^0, $V = 6.8 \times 10^{-5}$ eV and $\lambda = 0.14$ eV [82]. Knapp and Fischer criticized the use of these electronic parameters in view of the structure of *Rps. viridis*, and proposed yet another fit: $V = 3.7 \times 10^{-7}$ eV, $\hbar\omega_{\mathrm{m}} = 100$ cm^{-1}, $\lambda_{\mathrm{m}} = 0.12$ eV, $\hbar\omega_{\mathrm{i}} = 1000$ cm^{-1}, $\lambda_{\mathrm{i}} = 0.06$ eV [88]. Responding to that criticism, Bixon and Jortner revised the parameters of the parallel cytochrome oxidation mechanism and proposed a new set of parameters for the low-temperature activationless process ($\lambda = 0.50$–0.75 eV, $V = (1.6$–$5.0) \times 10^{-6}$ eV and $\hbar\omega_{\mathrm{m}} = 100$ cm^{-1}) and for the high-temperature activated process ($\lambda = 0.99$ eV, $V = 5.7 \times 10^{-4}$ eV) [95]. However, the implication that λ is now higher for the closest cytochrome is not satisfactory [96]. The parallel path mechanism was also criticized by Cartling on the basis that the cytochrome c of *Rb. sphaeroides* has a single heme but shows the same temperature dependence as *Cromatium* [97]. As an alternative, Cartling proposed a mechanism based on conformational control of ET. However, gating of ET by conformational transitions in proteins is unlikely in view of the 'uniform' electronic barrier to electron tunneling observed for the generality of biological ETs [6].

The complexity of Eqs. (1)–(7) and the diversity of fittings for the reduction of $\mathrm{P}^{\bullet +}$ by cytochrome c_2 illustrate the shortcomings of this theory, which is of limited guidance to the experimentalist. Actually, the initial charge-separation step can be fitted using the sequential mechanism as described above, or using a superexchange mechanism [33]. The multiparameter expression (1) does not give exact numerical values for λ or $\hbar\omega$ in each class of reactions [50]. A more favourable situation occurs in the temperature region where the thermal energy $k_{\mathrm{B}}T$ is much higher than $\hbar\omega$, the energy of the vibration coupled to ET, and Eq. (8) can be employed. In this case only two parameters, V and λ, need to be fitted to describe the ΔG^0 and temperature dependences of the reactions. This is the case of the $\mathrm{Q_B}^{\bullet -}$ to $\mathrm{P}^{\bullet +}$ charge recombination and $\mathrm{Q_A}^{\bullet -}$ to $\mathrm{Q_B}$ charge shift. A fit of Eq. (8) to the charge recombination between $\mathrm{Q_B}^{\bullet -}$ and $\mathrm{P}^{\bullet +}$ gave $V = 1.2 \times 10^{-3}$ cm^{-1} and $\lambda = 1.1$ eV [69]. However, in such cases the temperature dependence of the rates can be described by Arrhenius ($\ln k$ vs. $1/T$) and Eyring ($\ln (k/T)$ vs. $1/T$) plots, that also employ two parameters. This has been done for the $\mathrm{Q_A}^{\bullet -}$ to $\mathrm{Q_B}$ transfer [52].

Although the non-adiabatic ET theory can be used to fit the free-energy and temperature dependences of ET rates in RCs, it does not provide a method to calculate the parameters involved in the fittings and makes use of up to five adjustable parameters (V, λ_{m}, $\hbar\omega_{\mathrm{m}}$, λ_{i}, $\hbar\omega_{\mathrm{i}}$) and two mechanisms (superexchange versus sequential ET, two parallel oxidations) to reproduce the distance, free-energy and temperature dependence of each ET step in bacteria RCs. More specifically, it is of critical importance to calculate the electronic coupling between donor and acceptor, which apparently varies from 2.5×10^{-3} to 8.8×10^{-9} eV and accounts for variations in the rates of 11 orders of magnitude. The medium and intramolecular reorganization energies of these ETs, which range between 1.1 and 0.1 eV and lead to rate variations spanning four orders of magnitude at room temperature, should be calculated from the representation of the medium as a continuum dielectric and from the pertinent structural and spectroscopic data [84]. Finally, the role of the (medium and intramolecular) vibrational modes is deduced from an *a posteriori* analysis of the fittings.

3. Theory

The calculation of ET rates requires the use of two methods: one to calculate the barrier for electronic transmission from the electron donor to the acceptor (non-adiabatic factor), and the other to calculate the nuclear reorganization barrier (Franck–Condon factor). These two methods can be developed separately, in the spirit of the Born–Oppenheimer approximation. This separation is also used in the non-adiabatic multiphonon ET theory discussed above. However, our approach to calculate ET rates differs considerably from that theory. We first introduce simplified physical models that support our formulation of the ET rates, and then we calculate the rates without any further approximations. Our objective is to provide absolute estimates of all the ET rates occurring in the RC of *Rb. sphaeroides*, rather than to fit very closely the experimental rates by systematic adjustments of the model or its parameters.

3.1. Frequency factors

Bound systems oscillate about equilibrium positions. When such a system moves along a reaction coordinate, it will meet the reaction energy barrier in its motion. On each impact on that barrier there is a finite probability that the reactants escape and form the products, either because the reactants have enough energy to surmount the barrier or because they may tunnel through it. According to transition-state theory, the reaction coordinate is a very loose vibrational coordinate of the transition state that allows it to dissociate into the products. The rate constant of the reaction is the product of the concentration of transition states and the frequency of their decomposition. At room temperature, the frequency of that decomposition, $k_{\mathrm{B}}T/h$, corresponds to a vibration of 200 cm^{-1}. Outer-sphere ET reactions occur without the dissociation of any vibrational modes. The frequencies of the reactive bonds range from 200–500 cm^{-1} in metal–ligand bonds of metal complexes, to ca. 1600 cm^{-1} in double bonds of organic species. Thus, the nuclear frequencies in adiabatic ET reactions are in the range $\nu_n = 5 \times 10^{12} - 5 \times 10^{13}$ s^{-1}. This is much lower than typical electronic frequencies, which are usually taken as $\nu_{el} = 1 \times 10^{15}$ s^{-1}, and does not question the validity of the Born–Oppenheimer approximation. However, intermolecular ET occurs at distances larger than the sum of the van der Waals radii of the two reactants (3.6 Å) [6]. At this distance, a typical distance decay coefficient $\beta = 1.4$ Å^{-1} leads to a non-adiabatic electronic factor of $\chi_{el} = 0.0065$, i.e. the effective electronic frequency drops to $\chi_{el}\nu_{el} \leq 6.5 \times 10^{12}$ s^{-1}. The same limit is expected for intramolecular donor–spacer–acceptor systems, when the spacer is made up of more than two single CC bonds constrained to an extended configuration. This simple reasoning shows that in outer-sphere ET reactions the effective electronic frequency is of the same magnitude or smaller than the effective nuclear frequency.

The simultaneous involvement of nuclear and effective electronic frequencies in determining the frequency of an ET process is illustrated in Fig. 2. The frequency of the reaction is that of the approach to the reaction barrier. The crossing of the barrier follows the direction of the normal to the intersection between reactant and product representations. Fig. 2(a) shows the particular case where $\chi_{el}\nu_{el} = \nu_n$, and the frequency domains can be represented by circles. Presuming that there are no frequency shifts in the course of the reaction, the intersection of reactants and products occurs along the $y = x$ line. The normal to the circle representing the reactant frequency domain has a slope of unity, indicating that nuclear and effective electronic frequencies contribute equally to the impact of the system on the reaction energy barrier. Fig. 2(b) illustrates a non-adiabatic ET where $\nu_n = 5\chi_{el}\nu_{el}$. The intersection of the line $y = x$ with the ellipse representing the reactants and centered at the origin, $(x)^2/(\nu_n)^2 + (y)^2/(\chi_{el}\nu_{el})^2 = 1$, occurs at the point $y_1 = x_1 = \chi_{el}\nu_{el}\nu_n / [(\chi_{el}\nu_{el})^2 + (\nu_n)^2]^{1/2}$. The normal to the ellipse at this point has the slope of $(\chi_{el}\nu_{el})^2/(\nu_n)^2 = 25$.

In general, the contributions of the effective electronic and nuclear frequencies to the reaction frequency are given by

$$\nu = \chi_{el}\nu_{el}\,\mathrm{sen}\left[\mathrm{arctg}\left(\frac{\nu_n}{\chi_{el}\nu_{el}}\right)^2\right] + \nu_n \cos\left[\left(\frac{\nu_n}{\chi_{el}\nu_{el}}\right)^2\right] \qquad (9)$$

For the particular cases of Fig. 2(a) and 2(b), $\nu = \sqrt{2}/2(\chi_{el}\nu_{el} + \nu_n) = \sqrt{2}\chi_{el}\nu_{el}$ and $\nu = 0.999\chi_{el}\nu_{el} + 0.04\nu_n \approx 1.2\chi_{el}\nu_{el}$, respectively. The limit of $\chi_{el}\nu_{el}$ is attained for strongly non-adiabatic ET reactions. Using Eq. (9), the calculation of the effective frequency requires the knowledge of the nuclear frequency, the electronic frequency and the non-adiabatic factor. The nuclear frequency can be taken from the frequencies of the vibrational modes referred to above: $\nu_n = 6.4 \times 10^{12}$ s^{-1} for bacteriochlorophyll, 1×10^{13} s^{-1} for cytc, 5×10^{13} s^{-1} for aromatic systems and $(\nu_n)^2 = (^1/_2)[(\nu_{n,ox})^2 + (\nu_{n,red})^2]$ for mixed cases. The electronic frequency is $\nu_{el} \approx 1 \times 10^{15}$ s^{-1}. A method to calculate the non-adiabatic factor is discussed below. In practice, the reaction frequency ν in RCs does not exceed the value of $\chi_{el}\nu_{el}$ by more than a factor of 1.5. Therefore, the main factor controlling the reaction frequency ν is the electronic non-adiabatic factor χ_{el}. For all the ET reactions in the RCs considered in this work, we verified that $\nu \approx 10^{15}\chi_{el}$ s^{-1}, although our calculations made use of Eq. (9).

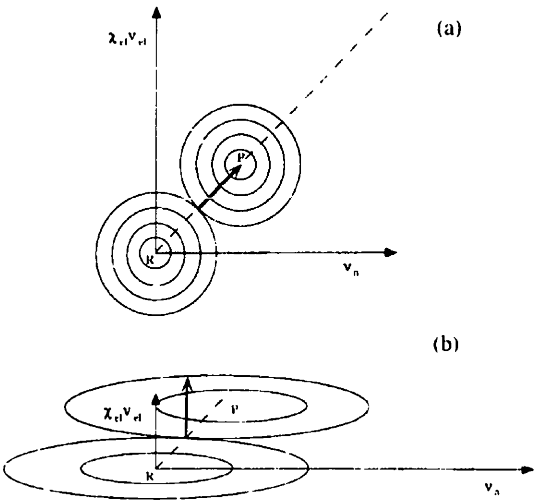

Fig. 2. Frequency domains of reactant (R) and product (P) in an electron exchange without frequency shifts. The horizontal axis represents the nuclear frequency (ν_n) and the vertical axis represents the effective electronic frequency ($\chi_{el}\nu_{el}$). The reaction frequency (ν) that effectively transforms the reactants in the products is represented by a thick arrow with a direction given by normal to the reactants curve at the intersection between R and P curves. Upper scheme, $\nu_n = \chi_{el}\nu_{el}$; lower scheme, $\nu_n = 5\chi_{el}\nu_{el}$.

A simple but reliable model to calculate the distance-dependent non-adiabatic factor has been presented in detail elsewhere [19,20]. In summary, the distance dependence of the electronic factor can be calculated as the permeability of a rectangular barrier in the WKB approximation

$$\chi_r = \exp\left[-\frac{2}{\hbar}\sqrt{2m_e\Phi}\,r_e\right] \qquad (10)$$

where m_e is the electron mass, r_e is the barrier length and Φ the barrier height. Given that the speed of light in a given medium (v) is related to its speed in the vacuum (c) through the refractive index of a medium (n_D), $v = c/n_D$, that energies are related to square of the velocities and that Maxwell relations can be used to obtain $\epsilon_{op} = (n_D)^2$, we suggested that

$$\Phi = \frac{\Phi_0}{\epsilon_{op}} \qquad (11)$$

where Φ_0 is the difference between the energy of the electron in the donor and its energy at rest in the vacuum. The value of Φ_0 for excited electrons in P* can be taken from the absolute potential of NHE ($\Phi_{NHE} = 4.44$ eV) [98], the electrochemical midpoint potential of P^+/P versus NHE ($E_m \approx 0.500$ V) and the excited state energy of P^* ($E_S = 1.39$ eV)

$$\Phi_0(P^*) = \Phi_{NHE} + E_m - E_S = 3.55 \text{ eV} \tag{12}$$

The Φ_0 values of each subsequent ET can be obtained from $\Phi_0(P^*)$ and the reaction free-energy difference between P^* and the corresponding ET step. The optical dielectric constant of proteins has been estimated to be close to that of amides, i.e. $\epsilon_{op} = 2.1$–2.2 [99]. We take the refractive index of formamide, $n_D = 1.45$, as the refractive index of the RCs at room temperature in all our calculations.

3.2. Equivalent intramolecular Franck–Condon factors

We will consider, as a first approximation, that the free-energy barrier for ET is dominated by nuclear displacements that originate mostly from the stretching of the reactive bonds. When the reactive bonds are approximated by harmonic oscillators, with force constants given by their vibrational frequencies, the nuclear reorganization energy is related to the distortions of these oscillators from their equilibrium positions to the transition-state configuration (Fig. 3). This representation of the unidimensional reaction coordinate (d) is related to the 'diabatic path' of Evans and Polanyi [100], proposed in the mid-1930s to locate the transition state of a bond-breaking–bond-forming process in terms of independent stretches of the internal coordinates of reactant and product. The sum of the j bond length changes can be written as

$$d = |l_1^{\ddagger} - l_{1,eq}| + |l_2^{\ddagger} - l_{2,eq}| + \ldots + |l_j^{\ddagger} - l_{j,eq}| \tag{13}$$

where $l_{1,eq}, l_{2,eq}, \ldots, l_{j,eq}$ are the equilibrium bond lengths of the j bonds involved in the reaction coordinate, and $l^{\ddagger}_1, l^{\ddagger}_2, \ldots, l^{\ddagger}_j$ are the corresponding bond lengths at the transition state configuration. A method to estimate such a reaction coordinate is provided by the intersecting-state model (ISM) [15,16,101].

The ISM was originally developed to calculate the rates of bond-breaking–bond-forming reactions. This model relates each reactive bond distortion, from an equilibrium to a transition state configuration, with the change in its bond order. Pauling's definition of bond order [102] is followed, and the reaction coordinate is approached in a similar manner to the BEBO model proposed by Johnston and Parr [103]. However, ISM incorporates two important features absent in other models. Firstly, when higher energy electronic configurations mix extensively with the lower energy configuration at the transition state, the transition-state bond order ($n^{\ddagger}$) used in ISM is enhanced relative to that expected from a simple bond-breaking process [104]. Secondly, ISM accounts for the dissipation of the reaction energy by non-reactive modes present in the molecule or in the medium, by including the effect of a mixing entropy parameter (Λ) in the reaction coordinate [105,106]. Under these conditions, it was shown that the sum of the reactive bond distortions is given by

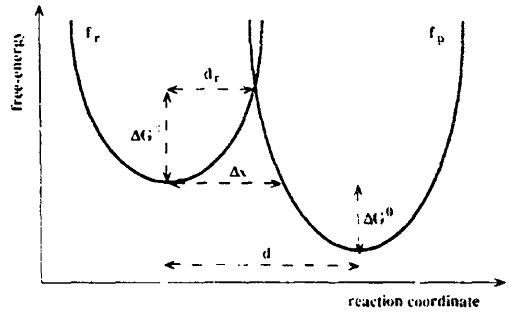

Fig. 3. Free-energy profile along the reaction coordinate defined by the ISM. Reactant and product are represented by harmonic oscillators with force constants f_r and f_p, respectively. The reaction coordinate d is given by the sum of the bond length changes from the equilibrium to the transition state configurations. The nuclear tunneling barrier width is represented by Δx.

$$d = (l_r + l_p)\frac{a'}{2n} \ln \frac{1 + \exp(\sqrt{2n}\,\Delta G^0/\Lambda)}{1 - [1 + \exp(\sqrt{2n}\,\Delta G^0/\Lambda)]^{-1}}) \tag{14}$$

were $a' = 0.156$ is a constant related to Pauling's 'universal' constant a [102]. When $\Delta G^0 \to 0$ or $\Lambda \to \infty$, Eq. (14) reduces to

$$d = (l_r + l_p)\frac{a' \ln(2)}{n} \tag{15}$$

Using the relations shown in Fig. 3, we have

$$\frac{1}{2} f_r d_r^2 = \frac{1}{2} f_p (d - d_r)^2 + \Delta G^0 \tag{16}$$

and the nuclear reorganization free-energy barrier is

$$\Delta G^{\ddagger} = \frac{1}{2} f_r d_r^2 \tag{17}$$

An important asset of this method is that the free-energy barrier ($\Delta G^{\ddagger}$) is related to known structural (equilibrium bond lengths l_r and l_p), spectroscopic (force constants f_r and f_p) and electronic (transition-state bond orders $n^{\ddagger}$) properties of the reactants and products, and to the thermodynamics of the reaction (free-energy ΔG^0). For very exothermic reactions ($\Delta G^0 < -50$ kJ mol^{-1}) the rates can only be rigorously calculated knowing the value of an energy dissipation parameter (Λ). This parameter is related to the coupling between reactive (reaction coordinate) and non-reactive (bath) modes. Strongly coupled modes behave statistically and the active modes of the nascent products are uncorrelated with the modes for activation of the reactants, except through conservation laws (energy, total angular momentum and its projection on one axis, linear momentum, electron spin angular momentum) and detailed balancing [107]. This situation is likely to occur if the potential gradients are smooth. In this case the reaction energy is statistically distributed among the bath modes and Λ is high [18]. Alternatively, if the potential gradients are large, the coupling is likely to be weak. In this case, vibrationally excited products are formed and A is low. For reactions in condensed media, the value of A is obtained from the phenomenological free-energy dependence of the reaction rates. Its value is expected to be constant for the same type of reactions in a given medium, because the potential gradients are similar. Lowering the temperature increases the rigidity of the system and may modify the coupling between reactive and medium modes. However, the protein medium of RCs is already rigid at room temperature [108], and the coupling in this system is not expected to be significantly temperature dependent.

The ISM has been extensively applied to atom-transfer [15], methyl group-transfer [109], hydride-transfer [110] and proton-transfer reactions [101,111–121]. The extension of the ISM from bond-breaking – bond-forming reactions to outer-sphere ET reactions, is based on the hypothesis that ET rates are determined by the bond rearrangements of the oxidized and reduced species prior to the transfer of the electron. If this is the case, the transition-state configuration coincides with the optimal Franck–Condon factors and the methodology employed by the ISM should be valid for both types of reactions. The sum of the bond distortions, d, represents the geometric requirements for the shift of an electron cloud and for the preparation of the reactants towards the equilibrium configuration of the products. This requirement is equivalent to the conservation of nuclei momentum and the ISM works as a universal scaling relationship for Franck–Condon factors.

The crucial difference between the application of the ISM to bond-breaking–bond-forming reactions

$$\mathrm{A{-}B + C \rightarrow A + B{-}C} \tag{I}$$

and to ET reactions,

$$R_{red}^{-}+R_{ox}\rightarrow P_{ox}+P_{red}^{-} \tag{II}$$

is the nature of $n^{\ddagger}$. In the former processes the bond order of AB decreases from unity in the reactants to zero in the products, while the opposite is happening to the bond order of the BC bond. In the absence of significant resonance with higher energy electronic configurations in the transition-state region, $n^{\ddagger}=0.5$. In ET reactions, we have to account for two reactants and two products. The sum of the bond orders of the reactants is identical to that of the products. Thus, the total bond order is preserved. For example, the bond order of p-benzoquinone is the average of the bond orders of two C=C double bonds, four C–C single bonds and two C=O double bonds, i.e. $n_{ox}=1.50$; on the other hand, its semiquinone radical has a smaller bond order because the extra electron is accommodated in an anti-bonding orbital delocalized over the conjugated system, $n_{red}=1.44$. The transition-state bond order is then $n^{\ddagger}=1.47$. In this approach we neglect the contribution of the CH bonds to the reaction coordinate because they are irrelevant for the orbitals involved in ET. Details on the calculations of $n^{\ddagger}$ for a wide range of organic molecules and transition-metal complexes can be found elsewhere [16–20]. For the purpose of this work, it is instructive to show how the transition state bond order of cytc must be estimated. The electronic interaction between the p-orbitals of the aromatic ligands and the d-orbitals of the metal lead to metal–ligand bonds with double bond character in the reactants with the configuration required for ET (Scheme 1). Thus we have $n^{\ddagger}=2$ for the Fe–N(aromatic) bonds. The bond order of the Fe–S bond can be estimated from the Gordy equation [122], which relates bond orders to force constants and bond lengths. Calibrating this equation with the relevant data from $\mathrm{Fe(OH_2)_6{}^{3+}}$ and $\mathrm{Fe(OH_2)_6{}^{2+}}$ complexes, we obtained $n^{\ddagger}=1.6$ for the Fe–S bonds [17]. With five transition state bond orders of 2 and one of 1.6, we obtain $n^{\ddagger}=1.93$ for cytc.

The ISM employs a unidimensional reaction coordinate defined only in terms of total bond distortions. The partition of those distortions by the reactive bonds is not uniquely defined. It is legitimate to take advantage of this feature and represent the reactants by an effective bond length and an effective force constant. The same can be done for the products. Eqs. (14) and (16) relate bond lengths and force constants to $n^{\ddagger}$ thus providing a criterion to reduce the dimensionality of the system. For the sake of consistency with the averaging procedure used to obtain $n^{\ddagger}$, we calculate the effective bond lengths as the average of the bond lengths involved in the reaction coordinate. For example, the average of the two C=C bonds ($l_{C=C}=1.322$ Å), four C–C bonds ($l_{C-C}=1.477$ Å) and two C=O bonds ($l_{C=O}=1.222$ Å) of p-benzoquinone [123], gives $l_{ox}=1.375$ Å. The same must be done to obtain l_{red} for the semiquinone radical. Then, the effective bond length of the reactants is

$$l_r=\frac{l_{ox}(\mathrm{B})+l_{red}(\mathrm{A}^{-})}{2} \tag{18}$$

The effective bond length of the products (l_p) is calculated in the same way. The same procedure is used to calculate the effective bond length of a metal complex. For example, cytc^{3+} has [124] $l_{\mathrm{Fe-N(His18)}}=2.00$ Å, $l_{\mathrm{Fe-S(Met80)}}=2.27$ Å and the average of the four $l_{\mathrm{Fe-N(heme)}}$ bonds is 2.055 Å, thus $l_{ox}=2.08$ Å. On the other hand, cytc^{2+} has [125]

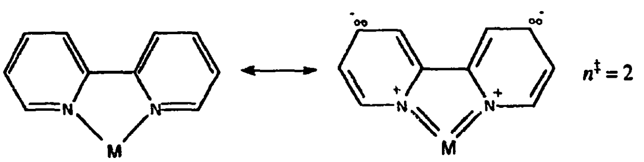

Scheme 1.

$l_{\mathrm{Fe-N(His18)}} = 1.97$ Å, $l_{\mathrm{Fe-S(Met80)}} = 2.32$ Å and an average $l_{\mathrm{Fe-N(heme)}} = 2.06$ Å, consequently $l_{\mathrm{red}} = 2.09$ Å.

The force constant of organic molecules can be obtained from normal coordinate analysis of their vibrational spectra. Bending modes are of much lower energy than the stretching ones, and their contribution to the reorganization energy is neglected. The effective force constant of an organic species can be obtained by a procedure similar to that described for the effective bond lengths, using only the stretching force constants of the reactive bonds. For example, p-benzoquinone has the following force constants (in 10^3 kJ mol^{-1} Å^{-2}) [126]: 5.48 (C=C), 2.81 (C–C) and 6.87 (C=O). Therefore $f_{\mathrm{ox}} = 4.49 \times 10^3$ kJ mol^{-1} Å^{-2}.

The force constants of the metal–ligand bonds in complexes are usually taken from their totally symmetric stretching frequencies, assuming that the ligand can be taken as a point mass [127,128]. The vibrational spectra of octahedral hexa-ammine complexes reveal the existence of small splittings between symmetric (ν_1) and antisymmetric (ν_3) metal–ligand stretching vibrations (20–40 cm^{-1}) [129], and weak metal-to-ligand force constants ($< 1.5 \times 10^3$ kJ mol^{-1} Å^{-2}) [17,130]. The splitting between ν_1 and ν_3 is related to the interbond coupling constant, $\epsilon = (\nu_1 - \nu_3)/2$ [131]. The weakness of the metal–ligand bonds leads to anharmonic effects at relatively low vibrational energies. The concurrence of weak coupling and anharmonicity suggests that metal–ligand bonds should be treated as local rather than as normal modes, because local mode behavior can be expected from small interbond coupling constants between anharmonic vibrational modes [131]. For example, the relatively harmonic OH bonds of the water molecule have $\epsilon = 50$ cm^{-1} and change from normal to local mode behavior at the third vibrational level [131]. One of us has shown how to calculate an effective force constant from the treatment of local modes as independent oscillators [132]. The diagonalization of the kinetic energy of the motions of the atoms in the molecule requires that, for a system of two oscillators in a molecule XYZ of atomic masses m_1, m_2 and m_3, the angle θ between the coordinate axes is given by

$$\cos\theta = \left[\frac{m_1 m_3}{(m_1+m_2)(m_2+m_3)}\right]^{1/2} \tag{19}$$

When the mass m_2 of the center-of-mass of the molecule is much larger than that of the ligand, $\cos\theta \approx 0$. Under these conditions, the force constant of an oxidized metal complex with j ligands is

$$f_{\mathrm{ox}} = \sqrt{[f_1(\mathrm{ox})]^2 + [f_2(\mathrm{ox})]^2 + \ldots + [f_j(\mathrm{ox})]^2} \tag{20}$$

where $f_1(\mathrm{ox}), f_2(\mathrm{ox}), \ldots f_j(\mathrm{ox})$ are the force constants of the j metal-to-ligand bonds of the reactant in the oxidized state. The same procedure is followed to calculate the force constant of the reactant in the reduced state, f_{red}. The force constant of the reactants is the average of the effective force constant of the reactants in the oxidized and reduced states

$$f_{\mathrm{r}} = \frac{f_{\mathrm{ox}}(\mathrm{B}) + f_{\mathrm{red}}(\mathrm{A}^-)}{2} \tag{21}$$

The same is done to calculate the force constant of the products. There is a contradiction between the arguments for a local mode behavior and the use of harmonic force constants. Harmonic force constants overestimate the energy require to distort the bonds and compensate for $\cos\theta \approx 0$, which slightly underestimates f_{ox} and f_{red}. The procedure to calculate the effective force constants of metal complexes can be illustrated using cytc as an example. The force constants of the Fe–N(histidine) bonds in cytc$^{2+/3+}$ should be similar to those of Fe–N(aromatic) bonds in Fe(bpy)$_3^{2+}$ and Fe(bpy)$_3^{3+}$ complexes, 1.42×10^3 and 1.44×10^3 kJ mol^{-1} Å^{-2}, respectively [17,18]. The Fe–N(pyrrole) force constants are assumed to be close to the Ni–N(pyrrole) force constants in nickel porphine, nickel tetraphenylporphine and nickel octaethylporphyrine, $f_{\mathrm{ox}} = f_{\mathrm{red}} \approx 3.52 \times 10^3$ kJ mol^{-1} Å^{-2} [133,134]. The Fe–S(Met80) force constant in cytc^{2+} and cytc^{3+} was estimated to be 1.44×10^3 kJ mol^{-1} Å^{-2} [135,136]. With these values we obtain $f_{\mathrm{ox}} \approx f_{\mathrm{red}} = 2.86 \times 10^3$ kJ mol^{-1} Å^{-2}.

Now that we have shown how to calculate $n^{\ddagger}$, l_{r}, l_{p}, f_{r} and f_{p}; we only need to know the value of Λ in order to calculate $\Delta G^{\ddagger}$ from Eq. (14)Eqs. (16) and (17). The exact value of Λ is only important for very exothermic reactions. Thus, the charge recombinations from $\mathrm{B_L}^-$ to P^+ and from $\mathrm{H}^{\cdot -}$ to $\mathrm{P}^{\cdot +}$ are sensitive to the value of Λ. The challenge of calculating the rates of all ET reactions in the RC without fitting any parameters can still be met if we take the value of Λ from earlier studies on photoinduced intramolecular ETs. These studies revealed that Λ should be in the narrow range of 100–140 kJ mol^{-1} [20]. In the present calculations we use $\Lambda = 130$ kJ mol^{-1}. Nearly identical results can be obtained with $\Lambda = 140$ kJ mol^{-1}, the value employed in the description of the ET rates in the paradigmatic systems studied by Closs et al. [137], and by Verhoeven et al. [138].

3.3. Nuclear tunneling

According to the thermodynamic formulation of transition-state theory, the rate of a chemical reaction such as Eq. (I) is given by

$$\begin{aligned} v &= \nu[\ddagger] = \nu[R_{\mathrm{red}}^-][R_{\mathrm{ox}}]K^{\ddagger} \\ &= \nu[R_{\mathrm{red}}^-][R_{\mathrm{ox}}]\exp\left(-\frac{\Delta G^{\ddagger}}{RT}\right) \end{aligned} \tag{22}$$

where ν is the frequency of vibration of the activated complexes in the degree of freedom corresponding to their decomposition, and $\Delta G^{\ddagger}$ is the increase in standard Gibbs free energy in the passage from the initial state to the activated state. The frequency of an ET reaction (II) is given by Eq. (9), with the distance-dependent non-adiabatic factor given by Eqs. (10) and (11). The configurational energy barrier is given by Eq. (17). Thus, the classical rate of an ET reaction, which corresponds to the rate of passage of the system over the top of the potential-energy barrier, can be calculated from the effective reaction frequency and the configurational barrier given by the ISM.

$$k_{ta}=\nu \exp\left(-\frac{\Delta G^{\ddagger}}{RT}\right) \tag{23}$$

For sufficiently low temperatures and significant barriers, the fraction of systems with enough energy to pass over the top of the energy barrier is negligible. Then, nuclear tunneling through the barrier may become the dominant reaction mechanism. We have shown that for barriers of the type shown in Fig. 3, the nuclear tunneling probability can be calculated from the WKB solution to a triangular barrier [139]. Even when the barriers are small, the Gamow factor can be accurately written as [139,140]

$$T=\frac{1}{1+\exp\left(\frac{1}{\hbar}\sqrt{2\mu\Delta E^{\ddagger}}\,\Delta x\right)} \tag{24}$$

where $\Delta E^{\ddagger}$ is the height and Δx the width of the tunneling barrier (Fig. 3). The calculation of tunneling effects using this formulation has found application in several systems [139,141].

The reduced mass of the system is determined on the assumption that the oxidized and reduced oscillators have common Δx and $\Delta E^{\ddagger}$ values [139]

$$\sqrt{\mu}=\sqrt{\mu_{ox}}+\sqrt{\mu_{red}} \tag{25}$$

The normal-mode analysis employed for organic molecules suggests that their reduced masses are the sum of the reduced masses of the independent oscillators in the molecule, i.e. benzoquinone: $\mu_{ox}=2\mu_{CC}+2\mu_{CO}$. Following the local-mode description of metal–ligand bonds of metal complexes, their reduced mass is given by the average of the reduced masses of all the independent metal–ligand bonds. When the mass of the center-of-mass is much higher that of the ligand, we have $\cos\theta\approx 0$ in Eq. (19), and the ligand vibrates against a still center of mass. Under these conditions, the reduced mass of the oscillator is just the mass of the ligand atom. For example, for cytc, $\mu_{red}=(5\mu_N+\mu_S)/6$.

The nuclear tunneling rate is given by the product of the effective reaction frequency by the barrier permeability

$$k_{nt}=\nu\frac{1}{1+\exp\left[\frac{1}{\hbar}\sqrt{2\mu\Delta E^{\ddagger}}\,\Delta x\right]} \tag{26}$$

The thermal activation rate (Eq. (23)) is appropriate for reactions taking place at sufficiently high temperatures (or reduced masses), when passage over the barrier dominates. At lower temperatures (or reduced masses), the nuclear tunneling rate (Eq. (26)) controls the kinetics of the system because the initial states preferentially escape through the barrier. The change from thermal activation to nuclear tunneling also depends on the energy of the barrier, because the thermal activation rate decreases exponentially with $\Delta G^{\ddagger}$ but the tunneling rate approximately decreases exponentially with $(\Delta E^{\ddagger})^{1/2}$. Finally, tunneling is also favoured by thin barriers, which result from high force constants and bond orders.

In order to describe the rates for all temperatures, reduced masses and barriers, let us consider what happens to a stream of particles with a Boltzmann energy distribution impinging on a one-dimensional energy barrier. The particles with more energy than the barrier height will normally cross over the barrier and contribute to the thermal activation rate. Only the particles with insufficient energy content to surmount the barrier, need be considered in the contribution to the nuclear tunneling rate. Thus, the quantum-mechanical rate constant of an ET reaction is given by

$$\begin{aligned} k&=\nu\left\{\exp\left(-\frac{\Delta G^{\ddagger}}{RT}\right)+\left[1-\exp\left(-\frac{\Delta G^{\ddagger}}{RT}\right)\right]\right.\\ &\qquad\left.\times\frac{1}{1+\exp\left[\frac{1}{\hbar}\sqrt{2\mu\Delta E^{\ddagger}}\,\Delta x\right]}\right\}\\ &=\nu\left\{\exp\left(\frac{-\Delta G^{\ddagger}}{RT}\right)+\left[1-\exp\left(-\frac{\Delta G^{\ddagger}}{RT}\right)\right]\right.\\ &\qquad\left.\times\frac{1}{1+\exp[2.226\sqrt{\mu\Delta E^{\ddagger}}\,\Delta x]}\right\} \end{aligned} \tag{27}$$

when μ is expressed in atomic mass units, $\Delta E^{\ddagger}$ in kJ mol^{-1} and Δx in Å.

Formally, the thermal activation barrier $\Delta G^{\ddagger}$ and the (zero-point energy corrected) tunneling barrier $\Delta E^{\ddagger}$ are related by

$$\Delta G^{\ddagger}=\Delta E^{\ddagger}+p\Delta V^{\ddagger}-T\Delta S^{\ddagger} \tag{28}$$

For condensed phases and not very high pressures, the term $p\Delta V^{\ddagger}$ can be neglected. For harmonic oscillators of different frequencies for reactants and products relatively small entropy changes are expected [142]. The main contribution to $T\Delta S^{\ddagger}$ is likely to come from changes due to restriction or freeing the orientations of solvent molecules. However, the rates of weakly exothermic ETs are nearly independent on non-specific solvent effects, as will be discussed below. Thus, $\Delta G^{\ddagger}$ and $\Delta E^{\ddagger}$ can be interchanged in Eq. (27), as has been done with ΔG^0 and ΔE^0 in Eq. (1) [72,83].

Another possible objection to the mixture of $\Delta G^{\ddagger}$ and $\Delta E^{\ddagger}$ terms in Eq. (27) is that thermal activation and nuclear tunneling follow different reaction coordinates. The tunneling path has been shown to correspond to a line of vibrational endpoints for reactions such as $H+H_2\rightarrow H_2+H$ [143]. Actually, this is also the reaction path we employ for ET reactions, because it maximizes the Franck–Condon factors. The tunneling path is a non-thermal path and may be less sensitive to the coupling between reactive and non-reactive modes. This may be manifested by different Λ values for thermal activation and nuclear tunneling paths. Except for the two very exothermic charge recombinations, the ET reactions in the RC are only weakly dependent on the value of Λ. Thus, in this work we assume that the thermal activation and nuclear tunneling barriers are identical.

3.4. Temperature dependence

The temperature dependence of the ET rates can be calculated from that of the parameters employed in the model. Bond lengths, force constants and bond orders are not expected to be appreciably temperature dependent. As discussed before, the dissipation of energy is unlikely to be appreciably temperature dependent in a protein medium. Furthermore, the observation of any variation of Λ with the temperature is restricted to strongly exothermic reactions, because only the rates of reactions with $\Delta G^0 < -50$ kJ mol^{-1} are sensitive to moderate variations in Λ. Of the ET reactions measured in the RC, only the charge recombination from $H_L^{\bullet -}$ to $P^{\bullet +}$ may reflect a temperature dependent Λ value. This is insufficient to justify a treatment of the temperature dependence of Λ at the present level of sophistication of our calculations. Therefore, we use $\Lambda = 130$ kJ mol^{-1} at all temperatures.

Proteins are known to contract as the temperature is lowered. For example, the linear thermal expansion coefficient of metmyoglobin is 115×10^{-6} K^{-1} [144], which is comparable to the coefficients measured for organic liquids. The situation in proteins is complicated by the fact that their thermal expansion is highly anisotropic. For simplicity, we assume that the linear thermal expansion coefficient of the RC is isotropic and equal to that of metmyoglobin, 115×10^{-6} K^{-1}. This coefficient is used to calculate the decrease in r_c as the temperature is lowered, which leads to an increase in the electron tunneling frequency via Eq. (10).

The refractive index of a medium increases with its density. Therefore, n_D in the present systems increases as the temperature is lowered. As the thermal expansion of a protein is similar to that of organic liquids, it is reasonable to assume that the temperature dependence of its refractive index is also similar to that of organic liquids. Typical values for these temperature dependences range between -0.00035 and -0.00055 K^{-1}. In our work we take the refractive index of formamide ($n_D = 1.45$ at room temperature) as that of the RC, and assume that its temperature dependence is -0.00045 K^{-1}. This gives, for example, $n_D = 1.55$ at 77 K. The increase in the refractive index also contributes to an increase in the electron tunneling frequency via Eq. (11).

3.5. The role of the medium modes

Presently most authors adhere to the current paradigms of ET theory, which takes the solvent reorganization energy as the major contributor to $\Delta G^{\ddagger}$ [145,146]. However, this classical perspective is being questioned [147–150] and we are seeing the emergence of the view that "Rates of outer-sphere ET reactions, particularly self-exchanges, are typically only marginally influenced by environmental factors" [151]. According to the models that describe the solvent as a dielectric continuum, the solvent reorganization contribution to $\Delta G^{\ddagger}$ is proportional to the Pekar factor ($\gamma = \epsilon_{op}^{-1} - \epsilon_s^{-1}$, where ϵ_{op} is the optical and ϵ_s is the static dielectric constant of the solvent), and to the reciprocal of the sum of the reactant radii [77,78,94]. In order to minimize electrostriction work in preassociation and probe directly the predictions of dielectric continuum models, it is convenient to discuss solvent effects on self-exchanges involving one uncharged species. Experiments with mixed solvents raise the problem that certain solutes will remain preferentially solvated and will not be considered here. We have recently shown that the solvent dependence predicted by such theories is not followed by electron self-exchanges of organic species [19]. Furthermore, the self-exchange reactions of alkylhydrazines$^{0/+}$ have nearly the same energy barrier in the vapour phase and acetonitrile solution [152]. Several self-exchanges of transition-metal complexes meeting the above conditions have also been studied: ferrocene/ferrocenium [$Fe(cp)_2^{0/+}$], cobaltocene/cobaltocenium [$Co(cp)_2^{0/+}$], tris(hexafluoroacetylacetonato)ruthenium(II/III) [$Ru(hfac)_3^{-/0}$] and bis-biphenylchromium(0/I) [$Cr(biph)_2^{0/+}$], as well as similar compounds with ligands bearing substituents. In Fig. 4 we have plotted the relative variations in the observed rate constants against the relative variations in the Pekar factor. We recall that dielectric continuum models predict that the solvent with the largest Pekar factor should yield the slowest ET rate. However, there is no apparent relationship between the relative rates, log (k/k_0), and the relative changes in the solvent parameter, $\gamma - \gamma_0$, where the index zero refers to the values measured in the solvent of highest Pekar factor.

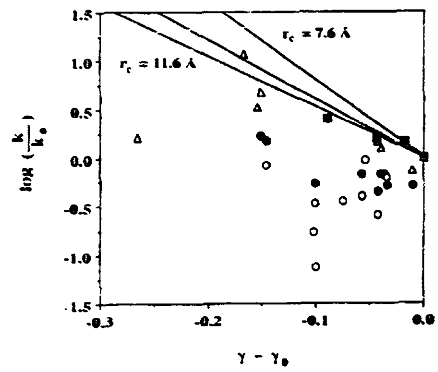

Fig. 4. Solvent dependence of self-exchanges of transition-metal complexes as a function of the solvent parameter $\gamma = n_D^{-2} - \epsilon^{-1}$. •, $Fe(cp)_2^{0/+}$; ○, $Co(cp)_2^{0/+}$; △, $Ru(hfac)_3^{-/0}$; □, $Cr(biph)_2^{0/+}$. The rates and solvent parameters are relative to the solvent with highest γ value, which Marcus theory predicts to give the slowest electron exchange rate. The lines were calculated with Marcus theory using center-to-center distances of 760 pm, 1000 pm and 1160 pm.

A closer inspection of Fig. 4 reveals that the rate of the $Fe(cp)_2^{0/+}$ exchange increases by a factor of 1.5 when the solvent is varied from methanol to benzonitrile (or nitrobenzene) [153] while at a center-to-center distance of 7.6 Å dielectric continuum models predict an increase by a factor of 15. The solvent dependence of the closely related $Co(cp)_2^{0/+}$ exchange deviates even more strongly from the dielectric continuum predictions for the same set of solvents: instead of the predicted 15-fold increase in rate, a decrease of 1.2 is observed [153]. Similarly, the rate of the $Ru(hfac)_3^{-/0}$ exchange increases by a factor of 4.9 when the solvent is changed from methanol to nitrobenzene while an 8.2-fold variation should be observed with a distance of 10.0 Å [154]. Even the self-exchange rate of $Cr(biph)_2^{0/+}$, often taken as the paradigmatic example of the solvent dependence predicted by dielectric continuum models [94,155], increases only by a factor of 2.5 when the solvent is changed from propylene carbonate to benzonitrile [156], while an increase by a factor of 3.1 is predicted with a side-side distance of 11.6 Å (with the head–head distance, 8.0 Å, a 5.2-fold increase is calculated). The discrepancy between the solvent effects predicted by dielectric continuum theories and the experimental values decreases with an increase in the center-to-center distance, i.e. the theory seems to be followed in the limit when it predicts nearly solvent independent rates. It should also be mentioned that the solvent dependence of the hexakis(cyclohexyl isocyanide)manganese(I/II) [$Mn(CNC_6H_{11})_6^{+/2+}$] self-exchange does not follow, even qualitatively, the predictions of the outer-sphere reorganization energy term of Marcus theory [157,158].

The effect of neglecting non-specific solvent effects in ET rates in symmetric systems can also be evaluated considering the solvent dependence of the low-energy absorption bands of mixed valence materials. Given the relation $E_{op}=4\Delta G^{\ddagger}$ between the energy of the intervalence band (E_{op}) and the free-energy barrier of the corresponding thermal ET [159], and the treatment of the solvent as a dielectric continuum, E_{op} should be proportional to $\gamma=\epsilon_{op}^{-1}-\epsilon_s^{-1}$. A careful study by Hupp et al. [160] of the solvent dependence of intervalence charge-transfer energetics in a prototypical mixed-valence system, [$(NH_3)_5Ru^{III}$-4,4′-bipyridine-$Ru^{II}(NH_3)_5$]$^{5+}$, in the limit of infinite dilution, shows that E_{op} varies from 114 kJ mol^{-1} in deuterium oxide ($\gamma=0.546$) to 93 kJ mol^{-1} in nitrobenzene ($\gamma=0.388$). A similar study by Nelsen et al. [161] on an organic intervalence compound led to $E_{op}=195$ kJ mol^{-1} in acetonitrile ($\gamma=0.526$) and 184 kJ mol^{-1} in CH_2Cl_2 ($\gamma=0.270$). The 10–20 kJ mol^{-1} variation in E_{op} with dramatic changes in the Pekar factor corresponds to a 2.5–5 kJ mol^{-1} variation in $\Delta G^{\ddagger}$, and substantiates our claim that non-specific solvent effects lead to less than 5 kJ mol^{-1} variations in $\Delta G^{\ddagger}$ values of thermal self-exchanges [20].

The experimental evidence on the gas phase reorganization energies and the solvent dependence of symmetrical thermal and optical ET of transition-metal complexes and organic species, strongly supports the view that outer-sphere ET rates are only marginally influenced by non-specific medium effects, and confirms our hypothesis that the free-energy barrier of electron self-exchanges in solution is dominated by intramolecular nuclear displacements. This idea is likely to work even better for ETs involving cofactors imbedded in a protein matrix, because the chromophores are surrounded by an essentially rigid protein medium and the electronic charge is spread over a large π-electron system in the donor and the acceptor. Warshel and coworkers [162,163] calculated the contribution of the protein reorientation to $\Delta G^{\ddagger}$ in the cytc self-exchange using structural information on ferro- and ferricytochrome c. According to their model, the contribution of the protein medium to the reorganization energy of cytc is much smaller than that expected for ET between two hemes in water. The medium reorganization energy was also neglected in the mechanism proposed by Kuhn and Kitzing [10,11]. It was once believed that the reorganization energy was likely to be small for biological redox partners, but detailed recent experiments show similar reorganization energies accompanying charge transfer in protein and normal solvents [164]. This is consistent with our hypothesis that the reorganization energies of ET process in biological systems are essentially determined by the reorganization energy of the cofactors, because non-specific medium effects are small contributors to $\Delta G^{\ddagger}$.

In exothermic ETs the solvent contributes to both the determination of the value of ΔG^0 and the accommodation of the exothermicity as the products are formed, thus it plays a role in the definition of the reaction coordinate. The actual role played by the solvent in these processes, which seemingly depends on the ΔG^0 of the ET reaction, has been a source of misunderstandings in the literature. In the framework of the ISM, an increase in solvent polarity contributes both to a change in the driving force of the ET reaction and to a stronger coupling between reactive and medium modes. In moderately exothermic ET reactions, the rates should increase with the solvent polarity because the driving force also increases, but this is compensated by an increase in d with $-\Delta G^0$. Experimentally, a weak solvent polarity dependence of mildly exothermic ('normal' region) photoinduced charge-separation rates is observed [165]. In very exothermic ('inverted' region) charge-shift reactions, the dissipation of the reaction free-energy will be facilitated by solvents strongly coupled with the reaction coordinate. Thus, more polar solvents should have higher Λ values. According to Eq. (14), in polar solvents (high Λ), d is relatively insensitive to $-\Delta G^0$ and fast rates are expected even deep into the inverted region. On the other hand, in a series of increasingly (very) exothermic reactions in weakly polar solvents (low Λ), d increases sharply with the driving force, dominates the usual decrease of $\Delta G^{\ddagger}$ with ΔG^0, and leads to slower ET rates. This explains why polar solvents give rise to faster rates than apolar solvents in the inverted region of intramolecular ETs [157,166]. This reasoning also helps to explains the difficulty in observing 'inverted' regions in intermolecular ET in polar solvents [167–169] and the stronger asymmetry of the free-energy

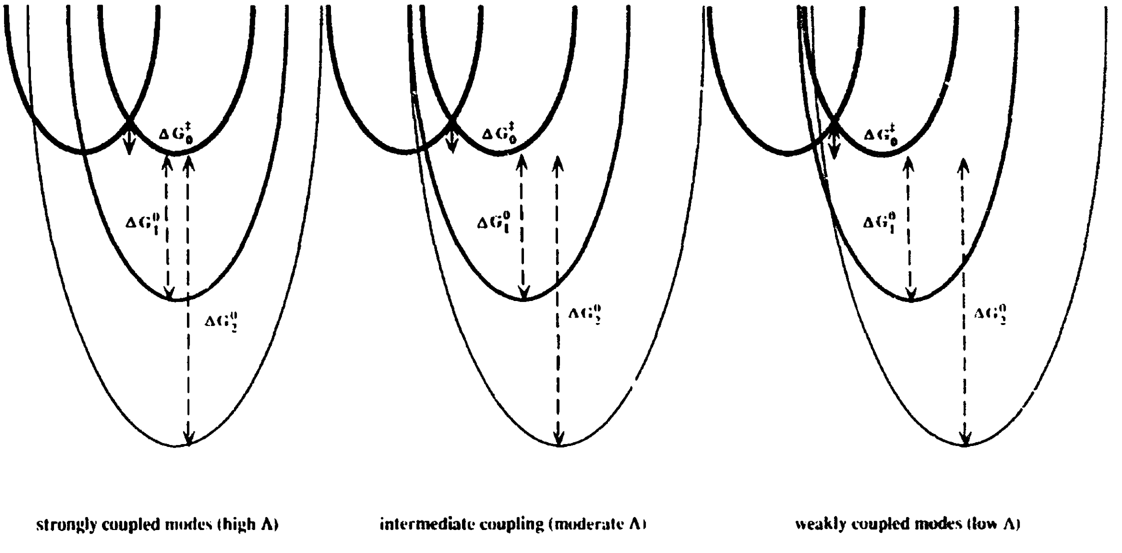

Fig. 5. Some particular cases of the relationships between ET rates and reaction free energies predicted by ISM. For strongly coupled modes (left), the intrinsic cross-reaction free-energy barrier ($\Delta G^{\ddagger}_{0}$) remains constant as the exothermicity of the reaction increases ($\Delta G^{0}_{2} < \Delta G^{0}_{1}$), and a bell-shaped Marcus inverted region should be observed. For an intermediate coupling between reactive and non-reactive modes (center), the decrease in reaction energy barriers with increasing exothermicities is compensated by a moderate increase in $\Delta G^{\ddagger}_{0}$, and the more exothermic reactions are nearly activationless. For weakly coupled modes (right) there is a dynamic restriction to the dissipation of the reaction free-energy that enhances the bond length changes, and an inverted region sets at moderate driving forces while the reaction rate barely attains the activationless limit.

dependence of ET in the more polar solvents [170,171]. The effects of high and low Λ values on ET rates are illustrated in Fig. 5.

4. Results

One of the most appealing features of the ISM is that once the reaction coordinate is defined, the ET rates can be calculated without any further approximations. The reaction coordinates of the nine types of ETs in the RC of *Rh. sphaeroides* can be obtained from the bond lengths, force constants and transition state bond orders of only four species: B (Mg–N bonds), H (CC and CN bonds of the bacteriochlorin core), Q_A (CC and CO bonds) and cytc (Fe–N and Fe–S bonds). The quinone and cytc data were discussed above. Typical Mg–N bond lengths are approximately 2.0 Å, as discussed before. We are not aware of the assignment of Mg–N vibrational frequencies in B, but a normal mode analysis of Ni^{II} porphyrins gave $f_{Ni-N} = 1.01 \times 10^3$ kJ mol^{-1} Å^{-2} [133,134]. Presuming that the ratio between f_{Ni-N} and f_{Mg-N} is equal to the $(\nu_{Ni-N}/\nu_{Mg-N})^2$ ratio, which is 1.80 in metalloporphyrins [172], we obtain $f_{Mg-N} = 0.56 \times 10^3$ kJ mol^{-1} Å^{-2}. Incidentally, the analogous ratio for aquo complexes [173] leads to $f_{Mg-N} = 0.59 \times 10^3$ kJ mol^{-1} Å^{-2}, hence this is a reliable procedure to obtain f_{Mg-N}. Using Eq. (20) and assuming that the histidine ligand is a true axial ligand of Mg^{II} in the special pair, we obtain $f_{red} = 1.25 \times 10^3$ kJ mol^{-1} Å^{-2}. However, it is likely that the excitation energy of P* does not activate all of its Mg–N bonds. If the reaction coordinate is determined by two Mg–N bonds in each reactant, the force constant of the oxidized and reduced species drops to 0.79×10^3 kJ mol^{-1} Å^{-2}. In the absence of data on the oxidized species, we presume that $f_{ox} = f_{red}$ for the special pair. The force constants of B_L can be calculated as those of P* but using its five Mg–N bonds. The transition-state bond order of the Mg–N(aromatic) bond is expected to be enhanced relative to its valence bond order [17,18,20], just as in the case of complexes with N-aromatic ligands such as the Fe–N(aromatic) bonds of cytc discussed before. Thus, we have $n^{\ddagger} = 2$.

The data needed to describe H was recently determined by Lin and Spiro [174]. The average of the CC and CN bond lengths of the bacteriochlorin core is $l_{ox} = 1.415$ Å, and, given the large size of the π-system, it is safe to assume that $l_{ox} = l_{red}$. Similarly, the average of the CC and CN force constants of the bacteriochlorin core is $f_{ox} = 3.43 \times 10^3$ kJ mol^{-1} Å^{-2}, and we can assume that $f_{ox} = f_{red}$. The average valence bond order of the bacteriochlorin core is $n_{ox} = 1.32$ and of its radical anion is $n_{red} = 1.30$, thus we have $n^{\ddagger} = 1.31$. Table 2 gathers all the information required by the ISM to determine the reaction coordinates of all types of ET reactions involved in the RC. The room-temperature rate constants can be calculated from that data, using the distances and free-energies shown in Fig. 1. Before presenting the application of the ISM to the calculation of the ET rates in the RC, it is instructive to see how the cofactors self-exchange rates are calculated.

In Table 2 we present the degenerate radical ion–neutral molecule electron exchange rates of bacteriopheophytin *a*

Table 2
ISM parameters required to calculate the ET rates in RCs (in italic) and the self-exchanges indicated

Couple	$\mu_{ox} \approx \mu_{red}$ [a] (a.m.u.)	$f_{ox} \approx f_{red}$ [b] (10^3 kJ mol^{-1} Å^{-2})	$l_{ox} + l_{red}$ [c] (Å)	$n^{\ddagger}$ [d]	ν_n (cm^{-1})	$E_{1/2}$ [e] (eV)	χ_{el} [f]	ν_t [g] (s^{-1})	T (K)	k_{ISM} [h] (M^{-1} s^{-1})	k_{se} (M^{-1} s^{-1})
P^*/P^+	*14.0*	*0.79* [i]	*4.00* [f]	*2.00*	*214* [k]	−0.97 [l]	8.4×10^{-3}	8.8×10^{12}	298	1.4×10^{12}	
$B_L^{\bullet-/0}$	*14.0*	*1.25* [m]	*4.00* [f]	*2.00*	*214* [k]	−0.99 [n]	8.5×10^{-3}	8.9×10^{12}	298	4.7×10^{11}	
$H_L^{0/\bullet+}$ or $P^{0/\bullet+}$	*73.9*	*3.43* [o]	*2.83* [o]	*1.31*	*1600*	0.82 [p]	3.0×10^{-3}	3.2×10^{12}	298	2.5×10^{8}	1.5×10^{8} [q]
$Q_A^{0/\bullet}$ or $Q_B^{0/\bullet-}$	*21.9*	*4.39* [i]	*2.76* [f]	*1.47*	*1600*	−0.52 [s]	6.3×10^{-1}	6.8×10^{12}	298	7.4×10^{6}	3.8×10^{8} [t]
$Fe^{3+/2+}$ (TPP) (MeIm)$_2$	14.0	2.86 [u]	4.00 [v]	2.00	385 [w]	1.02 [x]	3.1×10^{-3}	3.9×10^{12}	252	1.3×10^{9}	8×10^{7} [y]
$Fe^{3+/2+}$ cyt c	*17.0*	2.86 [z]	*4.17* [aa]	*1.93*	385 [w]	0.26 [ab]	1.2×10^{-6}	1.2×10^{9}	298	4.6×10^{5} [ac]	5.1×10^{3} [ad]

[a] Mass of the ligand in metal complexes and sum of the reduced masses of the oscillators in organic molecules.

[b] Using Eq. (20) for metal complexes and average of ring stretching force constants in organic species.

[c] From the average of the metal–ligand or aromatic ring bond lengths.

[d] From Ref. [18] for metal complexes or from Ref. [19].

[e] Reduction or oxidation potential, depending on how the couple was written.

[f] From Eq. (10), using $r_e = 8.9$ Å for $Fe^{3+/2+}$ cytc [175] and the van der Waals or interplanar distance $r_c = 3.5$ Å [6,176] for the other self-exchanges; the electron tunneling barrier was calculated from Eq. (11), given the absolute potentials of the reference electrodes, $\Phi_0 = 4.44$ eV for NHE [98] and $\Phi_0 = 4.71$ eV for SCE [177], and $\sqrt{\epsilon_{op}} = n_D = 1.45$.

[g] From Eq. (9) using $\nu_{el} = 1\times10^{15}$ s^{-1}.

[h] Using Eqs. (9), (15), (17) and (23).

[i] From the f_{Ni-N} in Ni^{II} porphyrins [134] and the ratio $(\nu_{Ni-N}/\nu_{Mg-N})^2$ in metalloporphyrins [172], using two Mg–N bonds.

[j] From Ref. [22].

[k] From metal–nitrogen frequencies in metal–porphyrin complexes [172].

[l] Excited state oxidation potential vs. SCE, from the oxidation potential, 0.42 vs. SCE [178], and excited state energy, 1.39 eV, of P*.

[m] From the f_{Ni-N} in Ni^{II} porphyrins [134] and the ratio $(\nu_{Ni-N}/\nu_{Mg-N})^2$ in metalloporphyrins [172], using five Mg–N bonds.

[n] From Ref. [178].

[o] From Ref. [174].

[p] Oxidation potential vs. SCE [178].

[q] In methanol–chloroform (1:3 v/v) [179].

[r] From p-benzoquinone [19].

[s] Reduction potential vs. SCE [180].

[t] In dimethylformamide [181].

[u] Assuming that $f_{Fe-N(pyrrole)} \approx f_{Ni-N(pyrrole)}$ and using the Ni–N(pyrrole) force constant given in Ref. [133], and from the ratio $(\nu_{Fe-N}/\nu_{Ru-N})^2$ in Fe(bpy)$_3^{2+/3+}$ [182] and Ru(bpy)$_3^{2+}$ [183] complexes and using the Ru–N force constant given in Ref. [184] as reference.

[v] From Ref. [185].

[w] From Ref. [182].

[x] Reduction potential vs. NHE estimated from data in Ref. [186].

[y] In CD_2Cl_2 [187].

[z] Using f_{Fe-N} as in $Fe^{3+/2+}$(TPP)(MeIm)$_2$ and f_{Fe-S} given in Ref. [135].

[aa] From heme iron co-ordination bond distances in both oxidation states of tuna cytochrome c [124,125].

[ab] Reduction potential vs. NHE [188].

[ac] Steric factors in the range 0.001–0.01 were proposed for this reaction [94,175].

[ad] Ionic strength of 0.1 M [189].

($H^{\bullet+/0}$) in 1:3 v/v methanol/chloroform (chlorophyll *a*, a model of $P^{\bullet+/0}$, has a similar rate) [179], *p*-benzoquinone$^{0/-}$ in *N,N*-dimethylformamide (an analogue of $Q_A^{0/-}$ and $Q_B^{0/-}$) [181], and Fe(TPP)(1-MeIm)$_2^{+/0}$ in CD_2Cl_2 (an 'adiabatic' cytc self-exchange model) [187]. These symmetrical exchanges have $\Delta G^0=0$ and their free-energy barriers can be calculated with Eqs. (15) and (17) making $d_r=d/2$. The reaction frequency is given by Eq. (9) and the non-adiabatic factor is determined by Eq. (10). The values of r_c for these reactions can be taken as the sum of the van der Waals radii or the interplanar distance in aromatic exciplexes, $r_c=3.5$ Å [6,176]. Using Eq. (27), we can calculate absolute rates for these reactions. The calculated rates are within an order of magnitude of the experimental ones. The horse-heart cytochrome c_2 self-exchange provides a most appropriate ground to test the calculation of the non-adiabatic factor in a symmetrical system. Using $E_m=0.26$ eV, $r_c=8.9$ Å, $n_D=1.45$, and Eqs. (10) and (11), we obtain $\chi_{el}=1.2\times10^{-6}$. The effective frequency of this reaction can be obtained simply from $\chi_{el}\nu_{el}=1.2\times10^9$, and the free-energy of activation is calculated in the same manner as for the other self exchanges. Using Eq. (27) we obtain $k_{ISM}=4.6\times10^5$ M^{-1} s^{-1}. The rate measured in aqueous solution with an ionic strength $I=0.1$ M is $k_{exp}=3.1\times10^3$ M^{-1} s^{-1} [189]. Two factors account for the difference between the calculated and experimental rates. Our calculations assumed that the heme-edge-to-heme distance of 8.9 Å can be applied to all mutual orientations of the two cytochromes in the ET complex, but only 0.7% of the cytc surface is heme [175]. Anisotropic bimolecular electron self-exchanges can take place from a variety of distances and orientations, and the calculated rates must be multiplied by steric factors specific to each system. Steric factors in the range 0.01–0.001 have been proposed for the cytc self-exchange [175]. Additionally, cytc self-exchange rates increase with the ionic strength [190]. The electrostatic work of approaching the two cytochromes was neglected in our calculations. Again, this quantity is anisotropic. Consideration of these factors would improve the agreement between calculated and experimental rates.

An assessment of the reorganization energy of the special pair can be made from its intravalence band. This has been observed at 2600 cm^{-1} in *Rb. sphaeroides* [191], which implies $E_{op}=31$ kJ mol^{-1} and $\Delta G^{\ddagger}=7.8$ kJ mol^{-1}. With the data in Table 2 and Eqs. (15) and (17) ($d_r=d/2$), we calculate $\Delta G^{\ddagger}=4.6$ kJ mol^{-1}. Using the five Mg–N bonds (1.25×10^3 kJ mol^{-1} Å^{-1}) leads to $\Delta G^{\ddagger}=7.5$ kJ mol^{-1}. Thus, the ISM calculates reliable Frank–Condon factors in ET processes. The nature of the electronically excited special pair and the very fast electron exchange rate expected for this system make it very difficult to find a bimolecular self-exchange that models its kinetics.

The main ambiguity in the application of the ISM to the calculation of ET rates in RCs rests in the contribution of the special pair to the reaction coordinate in the initial charge separation. An upper limit to the contribution of P* is given by the inclusion of five Mg–N bonds in the reaction coordinate, just like for B_L. A lower limit to that contribution can be estimated including only one of the P* Mg–N bonds in the reaction coordinate. This lower limit differs from the upper limit in two parameters: $f_r=f_p=0.91\times10^3$ kJ mol^{-1} Å^{-2} and $\mu=29$ a.m.u. This reduced mass was obtained from Eq. (24) knowing that Δx is the same for P* and B_L but that $\Delta E^{\ddagger}(P^*)=2/5\Delta E^{\ddagger}(B_L)$. The room-temperature time constants calculated for the initial charge separation using these limits are 1.4 and 3.6 ps. Using the sequential mechanism, time constants of 2.3 ps [41] and 3.1 ps [38] have been reported for this process. In the calculations presented in Tables 2 and 3 and in Figs. 6, 7 and 9 we represented P* by two Mg–N bonds, which is a compromise between the two limits.

The difficulty in the description of the special pair does not obscure the fact that our absolute rate calculations are in good agreement with the experimental rates of model self-exchanges. This agreement demonstrates that compensation of errors and parameter fitting are not crucial to the good performance of the theory.

Table 3
Reaction coordinates and ET rates [a] in *Rb. sphaeroides* RC

	r_c (Å)	ΔG^0 (kJ mol^{-1})	μ (a.m.u.)	Φ (eV)	$f_r\approx f_p$ (10^3 kJ mol^{-1} Å^{-2})	l_r+l_p (Å)	$n^{\ddagger}$	ν_n (cm^{-1})	k_{calc} (s^{-1})	k_{exp} (s^{-1})	Refs.
$P^*\rightarrow B_L$	4.7	−3.9	37	3.55	1.02	4.00	2.00	214	5.2×10^{11}	3.2×10^{11}	[38]
$B_L^{-}\rightarrow H_L$	3.8	−20.3	152	3.59	2.34	3.42	1.66	1141	5.3×10^{11}	6.7×10^{11}	[38]
$B_L^{\bullet-}\rightarrow P^{+}$	4.7	−130.3	37	3.59	1.02	4.00	2.00	214	2.2×10^9	$<7\times10^9$	
$H_L^{\bullet-}\rightarrow Q_A$	9.0	−62.7	176	3.80	3.91	2.80	1.39	1600	4.2×10^8	6.8×10^9	[38]
$H_L^{\bullet-}\rightarrow P^{\bullet+}$	10.0	−110.0	296	3.80	3.43	2.83	1.31	1600	2.1×10^8	5.6×10^7	[66]
$Q_A\rightarrow Q_B^{\bullet-}$	13.5	−5.8	88	4.45	4.39	2.76	1.47	1600	6.0×10^2	6.7×10^3	[54]
$Q_A^{\bullet-}\rightarrow P^{\bullet+}$	21.5	−47.3	176	4.45	3.91	2.80	1.39	1600	0.49	8.4	[67]
$Q_B^{\bullet-}\rightarrow P^{\bullet+}$	22.5	−41.5	176	4.51	3.91	2.80	1.39	1600	0.057	0.12	[69]
cyt c $\rightarrow P^{\bullet+}$	10.0	−15.4	162	4.78	3.48	3.48	1.62	1164	5.1×10^5	1.0×10^6	[59]

[a] The rate constants were obtained from the time constants given in the references, making use of the sequential mechanism.

[b] Energy of the electron in the donor relative to its energy in vacuum at rest: the electron tunneling barrier height is given by Eq. (11) using $n_D=1.45$.

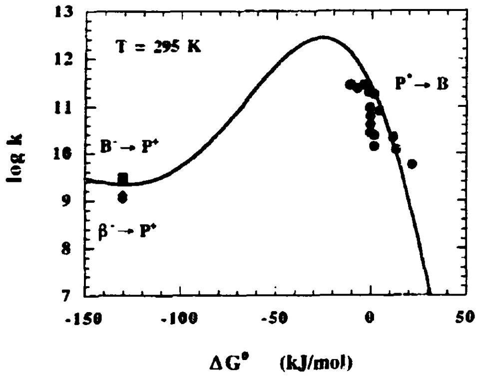

Fig. 6. Free-energy dependence of the ET rates, at room temperature, from P^* to B_L and from B_L to P^+, calculated with Eqs. (9), (14), (17), (27) and using the data for the $P^* \rightarrow B_L$ reaction coordinate in Table 3. ○, rates obtained from the reciprocal of the lifetimes of P^* in mutants, from Refs. [24,25,30,192–194]; □, upper limit for the $B \rightarrow P^+$ recombination rate that yields H with 99% efficiency; ◇, $\beta \rightarrow P^+$ recombination rates from Ref. [195].

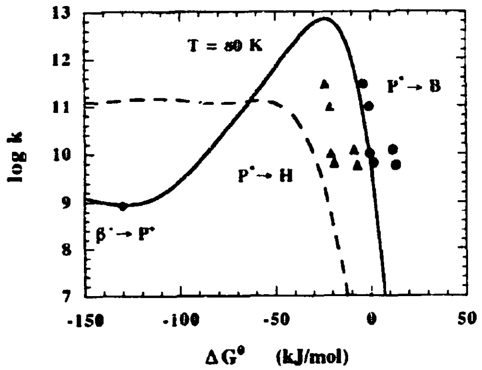

Fig. 7. Same as Fig. 6, but at 77 K. — calculations using the $P^* \rightarrow B_L$ reaction coordinate in Table 3; - - - calculations using the $P^* \rightarrow H_L$ reaction coordinate with two Mg–N bonds and the parameters for H_L given in Table 2 ($f_r = f_p = 2.00 \times 10^3$ kJ mol^{-1} Å^{-2}, $l_r + l_p = 3.42$ Å, $n^{\ddagger} = 1.66$, $\mu = 134$ a.m.u.) and $r_c = 7.3$ Å. The triangles represent the same lifetimes of P^* as the circles but reported to the free-energy difference between P^* and H_L.

Table 3 presents the reaction coordinates of the ET reactions in RCs. All of them were derived from the reaction coordinates of the self-exchanges in Table 2, using an averaging procedure. For the charge recombination $[P^+ B_L^-] \rightarrow [P B_L]$ two reaction coordinates can be envisaged. One is similar to the reaction coordinate for the charge separation $[P^* B_L] \rightarrow [P^+ B_L^-]$ and involves only the bacteriochlorophyll Mg–N bonds, whereas the other is defined by the Mg–N bonds of B_L and the CC and CN bonds of the bacteriochlorin core of P^+. The results presented in Table 3 refer to the use of the same reaction coordinate for charge separation and charge recombination between these two species. This seems to be the most reasonable choice, because these reactions take place on a picosecond time scale rendering the change in reaction coordinate very unlikely. The reaction coordinates of all the other ETs to the oxidized special pair were obtained from the CC and CN bonds of its bacteriochlorin core, and the oxidized special pair is intentionally represented as $P^{\cdot +}$. For these slower reactions, the contribution of $P^{\cdot +/0}$ to the reaction coordinate is identical to that of $H_L^{0/\cdot -}$. All the rates were calculated with $\Lambda = 130$ kJ mol^{-1} and are of the same order of magnitude as the experimental rates. The total charge-separation efficiency, reflecting the relation between charge-separation and charge-recombination rates of each step, reaches 66%.

The agreement between the calculated and experimental ET rates shown in Table 3 is remarkable. It depends on the empirical parameter Λ only for the very exothermic $B_L^- \rightarrow P^+$ and $H_L^{\cdot -} \rightarrow P^{\cdot +}$ recombinations. This encouraged us to calculate the free-energy and temperature dependences of all types of ET reactions taking place in bacteria RCs. These calculations are compared with experimental rates in Figs. (6)–(18). The model parameters required to obtain the profiles shown in these figures can be found in Table 3. The free-energies were obtained from the difference in the reduction potential of the electron donor or acceptor in the mutant or cofactor-reconstituted RC versus native RC. The temperature profiles include an isotropic contraction of the RC as the temperature is lowered, with the consequent linear increase in the refractive index, but the nuclear energy barriers were taken as temperature independent. The computed rates are the numerical result of the mathematics of our theories with the force constants, bond lengths, bond orders, nuclear frequencies and reduced masses gathered in Table 2 for the reactants of the ET reactions. We imposed $\Lambda = 130$ kJ mol^{-1} for all the systems addressed in this study. This value follows from our earlier work on intramolecular ET reactions [20]. The parameters of our model were not fitted to experimental kinetic data of the RCs.

5. Discussion

5.1. Primary electron transfer

The free-energy dependence of the initial ET step has been studied using mutations near the special pair to change its mid-point potential [25,30,192,193]. In three most endothermic reactions measured at room temperature, histidine (M)202 or (L)173 was replaced by leucine and the central Mg of the corresponding B was lost [24,194]. The result is a bacteriochlorophyll/bacteriopheophytin heterodimer primary electron donor. Fig. 6 compares the experimental rates with calculations using the $[P^* B_L] \rightarrow [P^+ B_L^-]$ reaction coordinate dictated by the Mg–N bonds (Table 3). At room temperature this reaction coordinate is dominated by thermal activation.

We also tested the 'superexchange' mechanism, in which the $[P^+ H_L^-] \rightarrow [P H_L]$ charge separation is mediated by the unoccupied orbitals of B_L, using the $P^* \rightarrow H_L$ reaction coordinate dictated by the data shown in Table 2. At room temperature and using $r_c = 7.5$ Å [195], 1 Å shorter than

$r_e(PB_L) + r_e(B_LH_L)$ due to the cofactor relative orientations and to $\chi_{el} \approx 1$ in the region occupied by H_L, the superexchange rate is a factor of 30 below the $[P^* B_L] \to [P^+ B_L^{\cdot -}]$ rates shown in Fig. 6.

Fig. 6 can also be used to investigate the room-temperature charge recombination $[P^+ B_L^{\cdot -}] \to [P B_L]$. Although such a process has not been directly studied, the near unit efficiency of the charge separation in RC requires that it is much slower than the charge shift $[B_L^{\cdot -} H_L] \to [B_L H_L^{\cdot -}]$. In Fig. 6 we represent by a square the recombination rate required for a 99% efficiency in the initial charge separation at the experimental charge-recombination free energy (− 1.34 eV). The efficiency of the initial ET step depends critically on the slowness of this reaction. Our calculations place the recombination rate in the free-energy region where it should be lower, and lead to a 99.6% charge-separation efficiency in this step. This figure also includes recombination rates of mutants that are discussed in the next section.

Fig. 7 shows the free-energy dependence of the initial charge-separation and charge-recombination rates at 80 K, along the $[P^* B_L] \to [P^+ B_L^{\cdot -}]$ reaction coordinate. At this temperature, the reaction mechanism is dominated by nuclear tunneling. The two endothermic rates shown in this figure were measured for heterodimers and are too fast for the ΔG^0 of a charge separation leading to $B_L^{\cdot -}$. This problem is not particular to the use of ISM, because the estimated endothermicity of 0.1 eV leads to Boltzmann factors of 2.0×10^{-2} at 298 K and 2.8×10^{-7} at 77 K, whereas the experimental rates in the heterodimers decrease by only a factor of 2 when the temperature is lowered from 298 to 77 K [194]. 'Superexchange' to H_L may help to explain the reactivity of these endothermic systems. The rates calculated with the reaction coordinate $[P^* H_L] \to [P^+ H_L^{\cdot -}]$ and $r_e = 7.3$ Å are three to four orders of magnitude lower than the experimental rates (dashed line in Fig. 7). Neglecting the contribution of P* to the 'superexchange' reaction coordinate and using $r_e = 7.3$ Å brings the calculated rates to within a factor of 100 of the experimental rates. Then, direct 'superexchange' to H_L becomes the dominant ET mechanism at low temperatures in heterodimer mutants. A similar change in mechanism also seems to be operative in a triple hydrogen bond RC mutant studied by Woodbury et al. [196], which has a P/P^+ midpoint potential 0.26 eV above wild type but gives a charge separation to the $[P^+ Q_A^{\cdot -}]$ with a quantum yield of 0.10–0.15 at 20 K. For the mutants with more exothermic initial ETs, the sequential mechanism is still dominant at low temperatures when compared with 'superexchange' over an effective distance of 7.3 Å.

We must emphasize that the kinetic analysis of transient spectra using a sequential, forward ET mechanism is not formally correct for the ET steps with $\Delta G^0 \approx 0$, because the reactant and product states of these steps are in equilibrium. Thus, the time constants fitted within such a mechanism in reactions with $\Delta G^0 > -5$ kJ mol^{-1} are not strictly comparable with the calculated first-order rate constants.

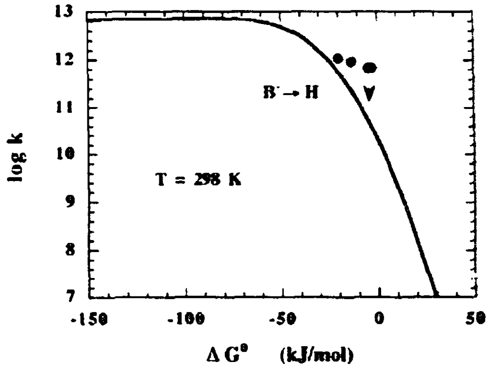

Fig. 8. Free-energy dependence of the ET rates, at room temperature, from $B_L^{\cdot -}$ to H_L, calculated with Eqs. (9), (14), (17), (27) and using the data for the $B_L^{\cdot -} \to H_L$ reaction coordinate in Table 3. Data from Ref. [48]. The rates with approximately zero driving forces are upper limits because the experimental kinetic scheme did not include reversibility.

The charge shift $[B_L^{\cdot -} H_L] \to [B_L H_L^{\cdot -}]$ in the native RCs is estimated to be slightly faster than the initial charge separation (Table 3). The driving force dependence of this ET rate was studied replacing H_L by pheophytin *a* [41], 3-acetyl-pheophytin *a* and 3-acetyl-bacteriopheophytin *a* [48]. The experimental and calculated rates are compared in Fig. 8. The charge-shift reactions with pheophytin *a* or 3-acetyl-bacteriopheophytin *a* in the H_L site were estimated to have ΔG^0 values in the −2 to −4 kJ mol^{-1} range and time constants of 1.5 ± 5 ps [48]. For such exothermicities, reversibility becomes important at room temperature and may change appreciably the time constants fitted to the transient spectra. For example, Holzwarth and Müller [38] obtained time constants of 1.5 and 2.5 ps using either a forward or a reversible model, respectively, to describe the charge shift $[B_L^{\cdot -} H_L] \to [B_L H_L^{\cdot -}]$ in the native RCs. These time constants and their differences are expected to be even larger in the modified RCs mentioned above, bringing the experimental rates into better agreement with the calculated ones.

The $[P^* B_L] \to [P^+ B_L^{\cdot -}]$ reaction coordinate can also be used to describe the temperature dependence of the P* state decay. Fig. 9 compares the experimental [27] and calculated temperature dependences of this system. The nuclear tunneling mechanism gives the correct increase in the ET rates as the temperature is lowered, although this is not apparent due to the contribution of thermal activation for the higher temperatures. For example, the ratio between the calculated tunneling rates at 8 and 293 K is 2.8, similar to the experimental ratio of 2.4 for *Rb. sphaeroides* and 3.7 for *Rps. viridis* [27].

The efficiency of the charge separation is close to unity at cryoscopic temperatures. This imposes an upper limit to the rates of charge recombination $[P^+ B_L^{\cdot -}] \to [P B_L]$ at very low temperatures. The calculations presented in Fig. 9 are consistent with a high charge-separation efficiency at low

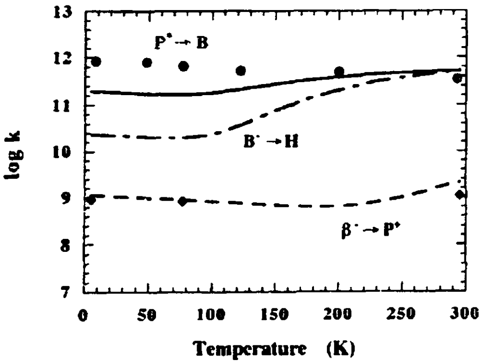

Fig. 9. Temperature dependence of the ET rates from P^* to B_L^- (———), from B_L^- to P^+ (- - -) and from B_L^- to H_L (— - —), calculated with the corresponding reaction coordinates given in Table 3. ○, from the lifetime of the special pair in Ref. [27]; ◇, from charge recombination in β mutants according to Ref. [195].

temperatures. This figure includes data on mutants to be discussed below.

We also investigated the temperature dependence of the charge shift $[B_L^-\ H_L] \rightarrow [B_L\ H_L^{\bullet -}]$. According to Fig. 9, the maximum of the ratio between the $[P^*\ B_L] \rightarrow [P^+\ B_L^-]$ and $[B_L^-\ H_L] \rightarrow [B_L\ H_L^{\bullet -}]$ reaction rates occurs near 77 K. Thus this should be the ideal temperature to look for the accumulation of B_L^- in the native RCs.

5.2. *Electron transfers from bacteriopheophytin*

The free-energy dependence of the $[H_L^{\bullet -}\ Q_A] \rightarrow [H_L\ Q_A^{\bullet -}]$ rate was extensively probed replacing the native ubiquinone-10 redox cofactor by quinone and non-quinone molecules [49,50]. The rate constants of this step were obtained from the yields of $Q_A^{\bullet -}$ formation, taking the rate of the $[P^{\bullet +}\ H_L^{\bullet -}] \rightarrow [P\ H_L]$ charge recombination as 7.7×10^7 s^{-1} at 295 K and 3.3×10^7 s^{-1} below 200 K. The yield of $Q_A^{\bullet -}$ formation with ubiquinone-3 at the Q_A site was taken as 0.984 at room temperature and 0.997 below 200 K. The free-energy profiles obtained at 295 and 14 K are compared with our calculations in Fig. 10. The largest discrepancies between calculated and experimental rates occur with 2,3,5-trimethyl-1,4-naphthoquinone in the Q_A site, which is also affected by the largest experimental uncertainty, and with ubiquinone-3, which has a tail of three isoprene units. The error bars included in the figure were taken from the work of Gunner and Dutton [50]. Dutton et al. have shown that long isoprenoid tails accelerate the rates of charge recombination from Q_A to $P^{\bullet +}$ at all temperatures [67]. The same acceleration should be observed in $[H_L^{\bullet -}\ Q_A] \rightarrow [H_L\ Q_A^{\bullet -}]$ step because the crystal structure of the RC shows that the isoprene units of the native ubiquinone are highly ordered and oriented towards H_L. Presumably such tails act as an antenna in the ET process and reduce the effective distance for ET. Thus, the fact that the experimental rate for ubiquinone-3 is ten

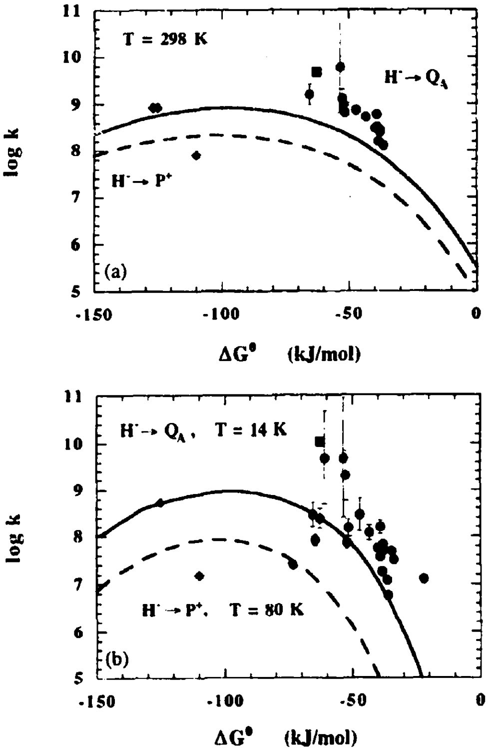

Fig. 10. Free-energy dependence of the ET rates from $H_L^{\bullet -}$ to Q_A (—, ○, □) and from $H_L^{\bullet -}$ to $P^{\bullet +}$ (- - -, ◇), calculated with Eqs. (9), (14), (17), (27) and using the $H_L^{\bullet -} \rightarrow Q_A$ and $H_L^{\bullet -} \rightarrow P^{\bullet +}$ reaction coordinates given in Table 3, respectively. ○, □, ubiquinone-3 in the Q_A site, data in Ref. [50]; ◇, data in Ref. [194]. a) 198 K; b) 14 K and 80 K.

times larger than the calculated one is an expected feature of our calculations which is entirely consistent with the results presented in Table 3. The rates calculated at 14 K are entirely due to nuclear tunneling.

Fig. 11 shows the temperature dependence of the ET rates with tetramethyl-1,4-benzoquinone and 1-amino-9-10-anthraquinone in the Q_A site. We selected these two examples to illustrate the temperature dependence of the $[H_L^{\bullet -}\ Q_A] \rightarrow [H_L\ Q_A^{\bullet -}]$ rates, because they correspond to the quinones with the largest differences in ΔG^0, -0.68 and -0.38 eV respectively, that Gunner and Dutton measured in the 14–295 K temperature range. The quantitative account of the temperature dependence of the rates of reactions with very different free energies, including the observation of a minimum ca. 120 K, is a remarkable feature of our model, especially because no parameters were adjusted in our calculations.

The rate of the $[P^{\bullet +}\ H_L^{\bullet -}] \rightarrow [P\ H_L]$ charge recombination determines the efficiency of $Q_A^{\bullet -}$ formation and the overall quantum yield of the charge separation in RCs. This charge-recombination rate has been measured in quinone reduced mutant RCs where the histidine in positions (L)173

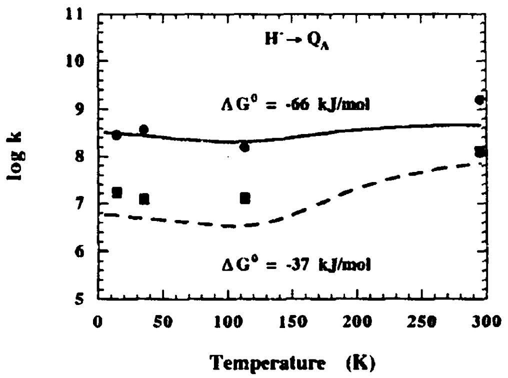

Fig. 11. Temperature dependence of the ET rates from $H_L^{\bullet -}$ to Q_A, calculated with Eqs. (9), (14), (17), (27) and using the $H_L^{\bullet -} \rightarrow Q_A$ reaction coordinate given in Table 3. ○, ———, tetramethyl-1,4-benzoquinone in the Q_A site; □, - - -, 1-amino-9,10-anthraquinone in the Q_A site. Data from Ref. [50].

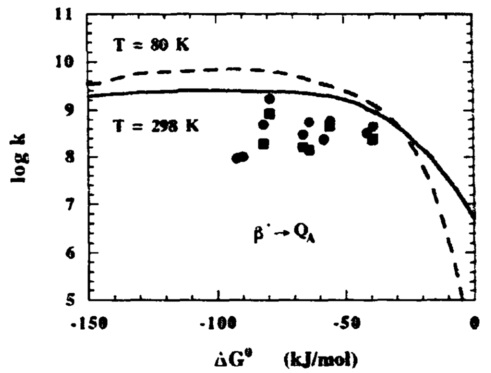

Fig. 12. Free-energy dependence of the ET rates from β^- to Q_A, calculated with Eqs. (9), (14), (17), (27), using $f_r = f_p = 2.82 \times 10^3$ kJ mol^{-1} Å^{-2}, $m = 71$ a.m.u., $l_r + l_p = 3.38$ Å and $n^{\ddagger} = 1.74$, and presuming that the reactive state is 290 J mol^{-1} above the non-reactive B_L^- state. ○, data at 298 K; ◇, data at 80 K. Data from Ref. [51].

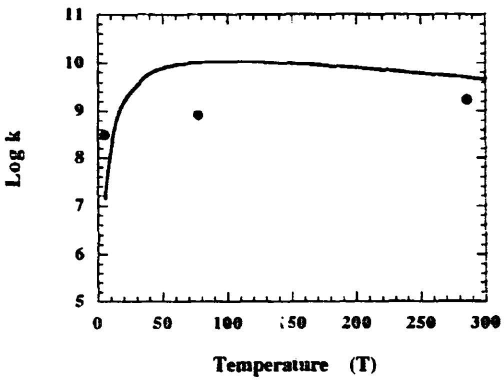

Fig. 13. Temperature dependence of the ET rates from b^- to Q_A, calculated as in Fig. 12. The data refers to the native quinone in the Q_A site [195].

or (M)202 were replaced by a leucine. Such mutations give B/H heterodimers with charge-recombination free energies of − 1.316 and − 1.298 eV, and rates of 8.3×10^8 s^{-1} at 295 K [194]. Fig. 10 shows the native ($\Delta G^0 = -1.14$ eV and 7.7×10^7 s^{-1} at 295 K) and heterodimer systems. The recombination rates calculated with $\Lambda = 130$ kJ mol^{-1} are intermediate between those of the native and mutant RCs. The calculated efficiency of $Q_A^{\bullet -}$ formation from $H_L^{\bullet -}$ is 67%. This is significantly below the near unity efficient observed in the native system. The main source of error is the underestimate of the $[H_L^{\bullet -}\ Q_A] \rightarrow [H_L\ Q_A^{\bullet -}]$ rate, which is 13 times lower than the experimental value. This can be explained by the neglect of the ubiquinone-10 isoprene tail, which is known to stimulate the ET rate. If a 10-fold increase in the charge-shift rate is included in our calculations to account for the presence of the isoprene tail in the native system, the calculated efficiency increases to 95%.

The change of leucine (M)214 to histidine leads to the replacement of the native H_L by a bacteriochlorophyll molecule, and this mutant has been denoted by β [51,65]. This mutant provides a stringent test of the reaction coordinates used in our study, because the charge shift to Q_A is now modelled by a different combination of the parameters shown in Table 2, but the charge recombination with P^+ follows the same $[P^+\ B_L^-] \rightarrow [P\ B_L]$ reaction coordinate. The energy of the $[P^+\ \beta^-]$ state lies slightly above that of the $[P^+\ B_L^-]$ state [65,195]. The charge shift to Q_A is expected to occur from the $[P^+ \beta^-]$ states in equilibrium with the $[P^+\ B_L^-]$ states, which decay by charge recombination to $[P\ B_L]$. The population of the $[P^+\ \beta^-]$ states should decrease dramatically at cryogenic temperature, and this should be reflected in the $[\beta^-\ Q_A] \rightarrow [\beta\ Q_A^{\bullet -}]$ rate. In fact, this rate decreases by only a factor of 5.5 when the temperature is reduced from 285 to 5 K. This argues in favour of very similar energies for the two states. In our calculations we assume that the $[P^+\ \beta^-]$ is 0.003 eV above the $[P^+\ B_L^-]$ state. In Fig. 12 we compare the free-energy dependence of calculated and experimental $[\beta^-\ Q_A] \rightarrow [\beta Q_A^{\bullet -}]$ rates. These calculations make use of the Boltzmann distribution between $[P^+\ B_L^-]$ and $[P^+\ \beta^-]$ states (0.47 at 298 K and 0.39 at 80 K), to account for the fraction of $[P^+\ \beta^-]$ states populated at these temperatures. A more impressive agreement with the experiment could be obtained if we had placed the $[P^+\ \beta^-]$ state 0.045 eV above the $[P^+\ B_L^-]$ state, as suggested by Kirmaier et al. based on dichroism data [195], because this energy difference gives Boltzmann factors of 0.15 at 298 K and 1.5×10^{-3} at 80 K. However, the temperature dependences of these rates, including the effect of the decrease in the population of the $[P^+\ \beta^-]$ state with the temperature, reveal that a large energy gap between the two states give negligible $[\beta^-\ Q_A] \rightarrow [\beta Q_A^{\bullet -}]$ rates at 5 K, which are not consistent with the experimental results, Fig. 13. The relatively fast rate at 5 K can be reconciled with low Boltzmann factors at higher temperatures, if the free-energy difference between the $[P^+\ \beta^-]$ and $[P^+\ B_L^-]$ states increases with the temperature. For example, a decrease by 0.001 eV in that free-energy difference leads to a factor of 10 increase in the rates at 5 K. Although it is reasonable to postulate a temperature-dependent equilibrium between these states and a precedent has been found in a RC reaction [52], we are reluctant to present a good fit for the free-energy and temperature dependences of the $[\beta^- Q_A] \rightarrow [\beta Q_A^{\bullet -}]$ rates based on a presumed temperature-dependent equilibrium, because we are committed to the calculation of ET rates in RCs without adjusting any parameters.

The charge recombination in the β-mutants occurs from B_L^- and follows the reaction coordinate discussed in relation to Fig. 6. Actually, this figure also includes the recombination rates of the β-mutants measured at 285 K [195]. The experimental rates are not strictly comparable with the calculations shown, because no provision was made for the slightly higher electron tunneling barrier of recombination rates or the fraction of B_L^- in the β-mutants. Both of these factors contribute towards a lower recombination rate in the β-mutants. The temperature dependence of these recombination rates [195] was included in Fig. 9. Again, the differences in the electron tunneling barrier and the population of the reactive states were neglected. It is superfluous to quantify these small corrections in a system where the contribution of the special pair to the reaction coordinate is not well defined.

5.3. Electron transfers from quinones

The rate of the charge shift from $Q_A^{\bullet -}$ to Q_B is accelerated by the presence of Fe^{2+} or any other divalent metal ion between the two quinones [54]. Actually, the ET rate calculated with our model (6.0×10^2 s^{-1}) is best compared with that of Fe-depleted RCs (2.9×10^3 s^{-1}), because we use $n_D = 1.45$ to represent the refractive index of the protein matrix at room temperature. Iron complexes have refractive indexes in the 1.5–1.7 range. Using $n_D = 1.6$ and $r_c = 13.5$ Å, we calculate a factor of 6.6 increase in the $[Q_A^{\bullet -}\ Q_B] \rightarrow [Q_A\ Q_B^{\bullet -}]$ rate relative to the calculations with $n_D = 1.45$ and $r_c = 13.5$ Å. This is more than the factor of 2.3 experimentally observed [54], and can be explained by the fact that the iron complex occupies a fraction of the distance between the two quinones.

The free-energy dependence of the $[Q_A^{\bullet -}\ Q_B] \rightarrow [Q_A\ Q_B^{\bullet -}]$ rate has been studied by varying the pH of the medium. ΔG^0 and the corresponding ET rate remain constant in the 6–9 pH range. Above pH 9, ΔG^0 increases to positive values, whereas the rate decreases proportionally with $[H^+]$ [68]. Both $Q_A^{\bullet -}$ and $Q_B^{\bullet -}$ associate with a proton, with pK values of 9.8 and 11.3, respectively [68]. The rates measured at pH > 9 are associated with changes in the protonation of the $Q_A^{\bullet -}$, and will not be considered further here. Dutton and coworkers [75,197] used quinone substitution to explore the free-energy dependence of this reaction. Their results are compared with our calculations in Fig. 14.

A temperature-dependence study of the $[Q_A^{\bullet -}\ Q_B] \rightarrow [Q_A\ Q_B^{\bullet -}]$ rate in the 278–303 K range [52], gave $A = 2 \times 10^{14}$ s^{-1} and $E_a = 60$ kJ mol^{-1}. Our calculations give $A = 1.8 \times 10^6$ s^{-1} and $E_a = 20$ kJ mol^{-1} and are illustrated in Fig. 15. It may not be legitimate to extend our calculations to very low temperatures, because it was shown that the free-energy of this charge shift becomes more negative as the temperature decreases [52] and this was not included in our calculations. The results of our calculations differ substantially from the experimental results of Mancino et al.. This is the only case of an ET reaction addressed in this work where our theoretical results disagree with the experimentalists view of the system. Given the exceedingly large A and E_a values obtained in the experimental study, we propose that the measured temperature dependence of the $[Q_A^{\bullet -}\ Q_B] \rightarrow [Q_A\ Q_B^{\bullet -}]$ rate does not reflect the activation of an elementary ET step, and support the suggestion that ET and protonation of Q_B are coupled [61], at least at low temperatures.

The free-energy and temperature dependence of the $[P^{\bullet +}\ Q_A^{\bullet -}] \rightarrow [P\ Q_A]$ charge recombination have been measured

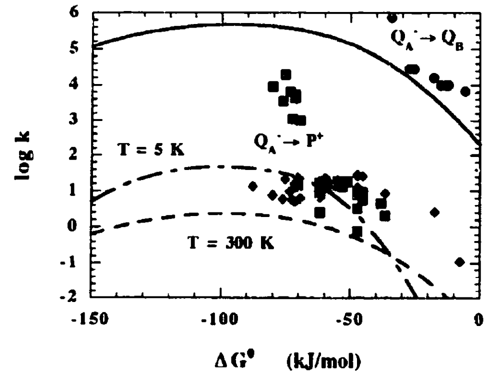

Fig. 14. Free-energy dependence of the ET rates from $Q_A^{\bullet -}$ to Q_B (——, ○) and from $Q_A^{\bullet -}$ to $P^{\bullet +}$ (- - -, □, ◇), calculated with Eqs. (9), (14), (17), (27) and using the reaction coordinates given in Table 3. ○, □, $T = 300$ K; ◇, $T = 5$ K. Data from Refs. [67,75,197,198]. The high $Q_A^{\bullet -} \rightarrow P^{\bullet +}$ rates of lower-potential quinones at room temperature are due to a change in mechanism.

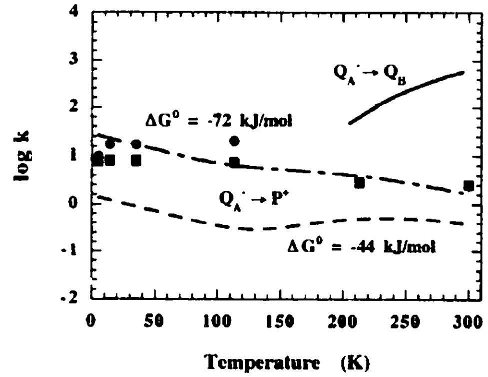

Fig. 15. Temperature dependence of the ET rates from $Q_A^{\bullet -}$ to Q_B (——), and from $Q_A^{\bullet -}$ to $P^{\bullet +}$ (- - -, □, ◇), calculated with Eqs. (9), (14), (17), (27) and using the reaction coordinates given in Table 3. ○, — - —, 2-methoxy-9,10-anthraquinone in the Q_A site; □, - - -, tetramethyl-1,4-benzoquinone in the Q_A site. Data from Ref. [67]. The rates measured for 2-methoxy-9,10-anthraquinone at $T > 100$ K are due to a change in mechanism and are not included in this figure.

replacing the native ubiquinone-10 by various quinones [67] and by site-directed mutagenesis around the special pair [198]. In Fig. 14 we compare the theoretical and experimental free-energy profiles at 300 and 5 K. The low potential quinones with $\Delta G^0 < -70$ kJ mol^{-1} have faster and temperature-dependent recombination rates above 100 K. This has been assigned to an indirect route for charge recombination [67], and will not be further considered. The rates calculated for the other quinones are in reasonable agreement with the experiment, especially considering the structural differences between the quinones and the presence of quinones with long isoprenoid tails, that enhance the rate of $P^{•+}$ reduction [67]. Two high-potential quinones (2,5-dichloro-3,6-dimethoxy-1,4-benzoquinone and 2,3-dichloro-1,4-naphthoquinone) were included in the free-energy profile at 5 K and seem to give exceedingly high rates for their ΔG^0 values. Part of the discrepancy may due to the differences between *in-vitro* and *in-situ* potentials, because the latter values are not available for these quinones.

The criterion discussed in the context of the $[H_L^{•-} Q_A] \to [H_L Q_A^{•-}]$ system, lead us to select tetramethyl-1,4-benzoquinone ($\Delta G^0 = -0.46$ eV) and 2-methoxy-9,10-anthraquinone ($\Delta G^0 = -0.75$ eV) [67] for the comparison between calculated and experimental temperature dependencies of $[P^{•+} Q_A^{•-}] \to [P Q_A]$ charge recombinations (Fig. 14). The relative temperature insensitivity of the direct recombination rates of these two systems, regardless of their 0.3 eV difference in ΔG^0, is adequately modelled by the theory without adjusting any parameters.

The efficiency of ET to $Q_B^{•-}$ can be estimated from the charge shift and charge recombinations discussed above. Using the data in Table 3 we obtain a theoretical efficiency of 99% at room temperature. The calculations of the temperature dependence of the charge-shift and charge-recombination rates in the native system reveal that its efficiency remains above 90% at cryogenic temperatures.

In native systems, the $[P^{•+} Q_B^{•-}] \to [P Q_B]$ charge recombination proceeds indirectly via the intermediate state $[P^{•+} Q_A^{•-}]$ [53]. The direct charge recombination was studied using mutant RCs in which asp (L)213 was replaced by asn to lower the energy of the $[P^{•+} Q_B^{•-}]$ state [53], or by replacing the native Q_A by low potential quinones [69]. In Fig. 16 we show the theoretical and experimental free-energy profiles of the direct recombination in RCs containing 2,3,6,7-tetramethyl-1,4-naphthoquinone in the Q_A site while retaining the native quinone in the Q_B site [69]. The free-energy variations result from changes in pH in the 6–10 range. The association of $Q_B^{•-}$ with a proton is not expected to change significantly in this pH range. The calculated and experimental rates are in excellent agreement. Charge-recombination rates of 0.10 and 0.13 s^{-1} were measured at 277 and 313 K, respectively, with the same exogenous quinone replacing the native quinone in the Q_A site [69]. The rates calculated with our model are 0.070 and 0.054 s^{-1}, respectively. Both these rates are dominated by thermal activation. The curious decrease in the rate with an increase in temperature is due to the thermal expansion of the RCs in an essentially activationless recombination rate. It seems that the presence of a nearby iron ion reduces the local thermal expansion of the RC.

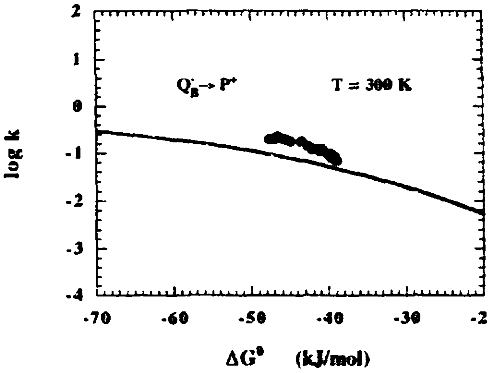

Fig. 16. Free-energy dependence of the ET rates from $Q_B^{•-}$ to $P^{•+}$, calculated with Eqs. (9), (14), (17), (27) and using the $Q_B^{•-} \to P^{•+}$ reaction coordinate given in Table 3. Data from Ref. [69].

5.4. Electron transfers from cytochrome c_2 to the RC

The relationship between rate and free-energy difference for the $[\mathrm{cytc}^{2+}\ P^{•+}] \to [\mathrm{cytc}^{3+}\ P]$ step has been investigated with a series of mutant RCs in which the midpoint potentials of the special pair were varied over a range of 0.35 eV [59]. In Fig. 17 we compare experimental and theoretical free-energy relationships for this reaction. The calculations were made with $r_c = 10$ Å, which is in the 9–14 Å range derived from RC–cytochrome complex models [59].

The temperature dependence of this reaction was measured in the 230–300 K range [63]. Below 238 K the special pair re-reduction cannot be followed experimentally. The theoretical and experimental rates are compared in Fig. 18. Actually, it is more informative to use the experimental data on *Chromatium* to evaluate the success of our model, because the rate constants in this system have been measured down

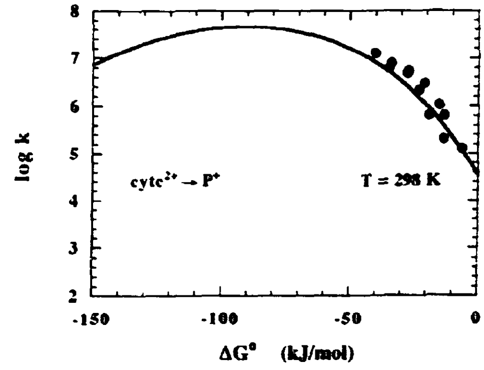

Fig. 17. Free-energy dependence of the ET rates from cytc^{2+} to $P^{•+}$, calculated with Eqs. (9), (14), (17), (27) and using the $\mathrm{cytc} \to P^{•+}$ reaction coordinate given in Table 3. Data from Ref. [59].

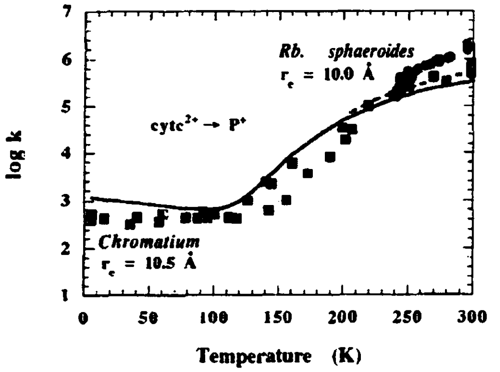

Fig. 18. Temperature dependence of the ET rates from $cytc^{2+}$ to $P^{\bullet +}$ in *Rb. sphaeroides* (○, - - -) and *Chromatium* (□, ———), calculated with Eqs. (9), (14), (17), (27) and using the cytc → $P^{\bullet +}$ reaction coordinate given in Table 3. ○, data from Ref. [63]; □, data from Refs. [21,91,92].

to 5 K. This is done in the same figure. As with all the other systems studied in this work, no parameters were fitted in the calculations presented in this figure. The edge-to-edge distance employed was intermediate between that used for *Rb. sphaeroides* (r_e = 10 Å), and that measured for *Rps. viridis* (r_e = 11 Å). The agreement between calculated and experimental rates cannot be simply dismissed as fortuitous. The force constants, bond lengths and bond orders employed for cytc were also used in self-exchanges presented in Table 2. Actually, the same Fe–N(histidine) data were also used to calculate self-exchanges and cross-reactions of iron complexes [17,18]. The force constants, bond lengths and bond orders of $P^{\bullet -}$ are the same as in three charge recombinations addressed in this study. The electronic non-adiabatic factor was calculated in the same manner as for all the other reactions presented in this study and for a large range of intramolecular ET reactions [20]. The reduced mass of this system was calculated using the methodology employed for all the other systems.

5.5. *Directionality*

The ET asymmetry, with preference for the transfer along the L-branch, in RCs with L and M branches related by an approximate C_2-symmetry, has been considered one of the most enigmatic properties of the RC [199]. The reasons for the selectivity can be attributed to three different causes.

The first and most investigated cause for the ET asymmetry is the energy positioning of the [$P^+ B_L^-$] and [$P^+ B_M^-$] states relative to [P* B]. Studies with mutants showed that the manipulation of one hydrogen-bonding interaction with one bacteriochlorophyll may change the relative energy of those states by 80–100 meV [24,199]. Calculations have placed the [$P^+ H_M^-$] state 90 meV above the [$P^+ H_L^-$] state [32]. We will take a more conservative approach and consider that the energy of [$P^+ B_M^-$] is 40 meV above that of [$P^+ B_L^-$], i.e. it is nearly isoenergetic with [P* B]. After all, the L and M subunits in *Rb. sphaeroides* have only about one-third of their amino acids residues in common [9], and the synergetic effect of many different, non-sequential amino acids may result is this modest energy difference. According to ISM, a 40 meV increase in ΔG^0 leads to a 2.3 times slower ET rate over the M-branch (k_M) than over the L-branch (k_L), at room temperature; with this difference in the driving forces, k_L/k_M increases to 32 at 80 K. The relatively steep dependence of the rates on ΔG^0 for nearly isothermic ETs was presented in Figs. 6 and 7.

The second cause invoked for the ET asymmetry is the dielectric asymmetry in the RC. More aromatic residues are found in the neighborhood of the B and H cofactors of the L-branch rather than of the M-branch [200], leading to a substantially higher dielectric strength along the L-branch [201]. In terms of our electron tunneling model, the lower dielectric constant of the M-branch leads to higher electron tunneling barrier via Eq. (11). If, for example, the optical dielectric constant of the M-branch is 1.82 (a value typical of a saturated hydrocarbon) whereas that of the L-branch is 2.1 (the value of formamide), then $k_L/k_M = 1.6$.

Finally, a cause that has not been considered in the analysis of the selectivity of ET in RCs, is the difference in Franck–Condon factors between the two branches. The magnesium–histidine nitrogen coordination distances are longer in the L-side of the special pair than in the M-side [22]. The same is true for the Mg–N(histidine) distances in the accessory bacteriochlorophylls [7]. These differences and the evidence presented previously that not all of the Mg–N bonds seem to contribute to the ET reaction coordinate, suggest that an additional Mg–N bond may be included in the reaction coordinate along the M-branch. This additional Mg-bond leads to $k_L/k_M = 1.3$.

The joint effect of the three causes discussed above leads to $k_L/k_M = 4.8$ at room temperature, in good agreement with the experimental limit of > 5 [32]. Thus, at room temperature, only 15% of the electrons transfer over the M-branch. At 80 K this ratio increases to more than 60, consistent with the experimental values of > 25 [33] and > 200 [34]. The temperature dependence of the selectivity of the initial ET is shown in Fig. 19.

6. Conclusions

The agreement between calculated and experimental ET rates shown in Figs. (6)–(19) was obtained without fitting any parameters. The 13 orders of magnitude breadth in the rates of the nine types of ET reactions is the outcome of their differences in force constants, bond lengths, bond orders, reduced masses, reaction free-energies and distance-dependent non-adiabatic factors. They have in common the electronic frequency ($\nu_{el} = 10^{15}$ s^{-1}), refractive index ($n_D = 1.45$), coupling between reactive and non-reactive modes ($\Lambda = 130$ kJ mol^{-1}) and thermal expansion. The success of our theoretical modelling is due to:

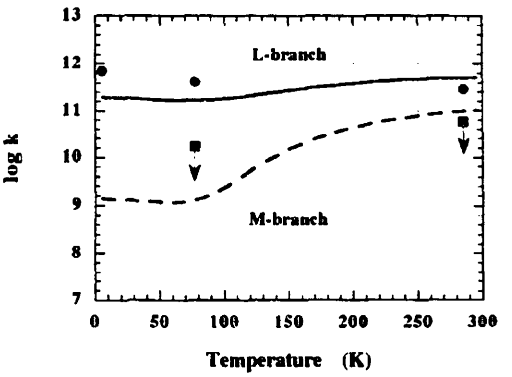

Fig. 19. Temperature dependence of the ET rates from P* to B_L^- (——) and from P* to B_M^- (- - -). The rates along the L-branch were calculated with $f_r = f_p = 1.02 \times 10^3$ kJ mol^{-1} Å^{-2}, $\mu = 37$ a.m.u., $l_r + l_p = 4.00$ Å, $n^{\ddagger} = 2.00$ and $\chi_{el}\nu_{el} = 1.9 \times 10^{12}$ s^{-1}. The rates along the M-branch were calculated with $f_r = f_p = 1.11 \times 10^3$ kJ mol^{-1} Å^{-2}, $\mu = 44$ a.m.u., $l_r + l_p = 4.00$ Å, $n^{\ddagger} = 2.00$ and $\chi_{el}\nu_{el} = 1.2 \times 10^{12}$ s^{-1}. ○, data from Ref. [195]; □, data from Refs. [32] and [33].

(i) the accuracy of our electron tunneling model (Eqs. (10) and (11)) in estimating the non-adiabatic factors of ET across edge-to-edge distances ranging from 3.8 to 22.5 Å;

(ii) the use of the ISM (Eqs. (14)-(17)) to estimate the Franck-Condon factors of ET reactions proceeding by thermal activation and nuclear tunneling mechanisms;

(iii) the appropriateness of $\lambda = 130$ kJ mol^{-1}, taken from earlier applications of the ISM, to describe the ΔG^0 dependence of the rates;

(iv) the changeover from thermal activation to nuclear tunneling at lower temperatures, modulated by the value of μ.

Our calculations show that the high efficiency of the RCs is achieved through a detailed control of the distance-dependent non-adiabatic factor. The distance between donor and acceptor for each forward charge-separation reaction is always shorter than the distance for the competing back reactions. Furthermore, the rates of the charge-separation reactions are enhanced by fine structural details, like the long isoprenoid tail of ubiquinone in the Q_A site with at least six highly ordered isoprene units oriented toward H_L, or the presence of an ion complex with high n_D between Q_A and Q_B. Only in the case of the first ET step does the RC take advantage of the inverted region to reduce the rate of the charge-recombination reaction. The other charge recombinations are not sufficiently exothermic to fall in the inverted region. Including the 10-fold increase in the ET rates to and from Q_A due to its isoprenoid tail, our calculations give a 94% charge-separation efficiency in *Rb. sphaeroides* reaction centres.

The selective ET along the L-branch results from a cocktail of energetic, electronic and structural factors. The advantage of the functional asymmetry of the RC may be explained by the fact that Q_B^- needs to picks up a second electron and two protons to form Q_BH_2 and dissociate from the RC. The processes initiated by the electronic excitation of the special pair lead to the formation of Q_A^- in less than 1 ns. The re-reduction of the special pair by the exogenous cytc takes place with a time constant of 1 µs. If the two branches were equally operative, 1 µs would also be the time constant for the formation of Q_B^{2-}. By sending the electron preferably over the L-branch, the time constant for the formation of Q_B^{2-} (or an equivalent protonated form) is slowed down to 150 µs or more, because the second electron is likely to be transferred more slowly than the first one from Q_A^- to Q_B^-. It seems that Q_A^- is a 'parking state' for the second electron, because it sustains a charge separation for a long time, enough to couple electron and proton transfer to Q_B^-. Such coupling of electron and proton transfers, with the associated conformational changes, would explain the pre-exponential factor and activation energy barrier observed for this step. The protonation of Q_B^{2-} is necessary for the unbinding of the quinone from the RC protein and its diffusion through the lipid bilayer to the cytochrome b/c_1 complex. However, the rate of this protonation is limited by the availability of protons near the Q_B site. The long lifetime of Q_A^- facilitates the proton recovery around the Q_B site. The turnover half-time of the Q_B site is about 3 ms [202].

We can only speculate about the function of B_M and H_M. The presence of a carotenoid close H_M and its ability to deactivate the triplet state of tetrapyrrolic molecules, suggests that B_M and H_M may channel to the carotenoid the energy of any triplets formed in the L-branch, and prevent the formation of singlet oxygen [202].

Acknowledgements

We thank Junta Nacional de Investigação Científica and Praxis XXI Programme (European Union) for financial support: project no. PRAXIS/2/2.1/QUI/390/94.

References

[1] G. Porter, in A. Zewail (ed.) The Chemical Bond. Structure and Dynamics, Academic Press, San Diego, CA, 1992, p. 113.

[2] J. Deisenhofer, O. Epp, K. Miki, R. Huber, H. Michel, J. Mol. Biol. 180 (1984) 385.

[3] J. Deisenhofer, O. Epp, K. Miki, R. Huber, H. Michel, Nature, 318 (1985) 618.

[4] C.H. Chang, D. Tiede, J. Tang, U. Smith, FEBS Lett. 205 (1986) 82.

[5] J.P. Allen, G. Feher, T.O. Yeates, H. Komiya, D.C. Rees, Proc. Natl. Acad. Sci. USA 84 (1987) 5730.

[6] C.C. Moser, J.M. Keske, K. Warncke, R.S. Farid, P.L. Dutton, Nature 355 (1992) 796.

[7] O. El-Kabbani, C.-H. Chang, D. Tiede, J. Norris, M. Schiffer, Biochemistry 30 (1991) 5361.

[8] J. Deisenhofer, O. Epp, I. Sinning, H. Michel, J. Mol. Biol. 246 (1995) 429.

[9] A.K.W. Taguchi, J.E. Eastman, D.M. Gallo, Jr., E. Sheagley, W. Xiao, N.W. Woodbury, Biochemistry 35 (1996) 3175.

[10] H. Kuhn, Phys. Rev. A 34 (1986) 3409.

[11] E.v. Kitzing, H. Kuhn, J. Phys. Chem. 94 (1990) 1699.

[12] S. Efrima, M. Bixon, Chem. Phys. Lett. 25 (1974) 34.

[13] R. Kubo, Y. Toyozawa, Prog. Theor. Phys. 13 (1955) 160.

[14] T. Holstein, Ann. Phys. 8 (1959) 325.

[15] A.J.C. Varandas, S.J. Formosinho, J. Chem. Soc. Faraday Trans. 2 82 (1986) 953.

[16] S.J. Formosinho, in S.J. Formosinho, I.G. Csizmadia, L.G. Arnaut (eds.), Theoretical and Computational Models for Organic Chemistry, NATO ASI, Kluwer, Dordrecht, 1991, p. 159.

[17] S.J. Formosinho, L.G. Arnaut, J. Mol. Struct. (Theochem.) 130 (1994) 105.

[18] S.J. Formosinho, L.G. Arnaut, J. Photochem. Photobiol. A: Chem. 82 (1994) 11.

[19] S.J. Formosinho, L.G. Arnaut, Bull. Chem. Soc. Jpn. 7 (1997) 977.

[20] L.G. Arnaut, S.J. Formosinho, J. Photochem. Photobiol. A: Chem. 100 (1996) 15.

[21] D. DeVault, B. Chance, Biophys. J. 6 (1966) 825.

[22] A.J. Chirino, E.J. Lous, M. Huber, J.P. Allen, C.C. Schenck, M.L. Paddock, G. Feher, D.C. Rees, Biochemistry 33 (1994) 4584.

[23] J.O. Goldsmith, B. King, S.G. Boxer, Biochemistry 35 (1996) 2421.

[24] L.L. Laporte, V. Palaniappan, D.G. Davis, C. Kirmaier, C.C. Schenck, D. Holten, D.F. Bocian, J. Phys. Chem. 100 (1996) 17696.

[25] V. Nagarajan, W.W. Parson, D. Davis, C.C. Schenck, Biochemistry 32 (1993) 12324.

[26] N.W. Woodbury, W.W. Parson, Biochim. Biophys. Acta 850 (1986) 197.

[27] G.R. Fleming, J.L. Martin, J. Breton, Nature 333 (1988) 190.

[28] V. Nagarajan, W.W. Parson, D. Gaul, C. Schenck, Proc. Natl. Acad. Sci. USA 87 (1990) 7888.

[29] P. Hamm, K.A. Gray, D. Oesterhelt, R. Feick, H. Scheer, W. Zinth, Biochim. Biophys. Acta 1142 (1993) 99.

[30] L.M.P. Beekman, I.H.M. van Stokkum, R. Monshouwer, A.J. Rijnders, P. McGlynn, R.W. Visschers, M.R. Jones, R. van Grondelle, J. Phys. Chem. 100 (1996) 7256.

[31] S. Lin, W. Xiao, J.E. Eastman, A.K.W. Taguchi, N.W. Woodbury, Biochemistry 35 (1996) 3187.

[32] M.E. Michel-Beyerle, M. Plato, J. Deisenhofer, H. Michel, M. Bixon, J. Jortner, Biochim. Biophys. Acta 932 (1988) 52.

[33] M. Bixon, J. Jortner, M.E. Michel-Beyerle, A. Ogrodnik, Biochim. Biophys. Acta 977 (1989) 273.

[34] E.C. Kellogg, S. Kolaczkowski, M.R. Wasielewski, D.M. Tiede, Photosynthesis Res. 22 (1989) 47.

[35] M. Marchi, J.N. Gehlen, D. Chandler, M.J. Newton, J. Am. Chem. Soc. 115 (1993) 4178.

[36] N.W. Woodbury, J.M. Peloquin, R.G. Alden, X. Lin, S. Lin, A.K.W. Taguchi, J.C. Williams, J.P. Allen, Biochemistry 33 (1994) 8101.

[37] C. Kirmaier, D. Holten, Biochemistry 30 (1991) 609.

[38] A.R. Holzwarth, M.G. Müller, Biochemistry 35 (1996) 11820.

[39] R.G. Alden, W.W. Parson, Z.T. Chu, A. Warshel, J. Am. Chem. Soc. 117 (1995) 12284.

[40] K. Dressler, E. Umlauf, S. Schmidt, P. Hamm, W. Zinth, S. Buchanan, H. Michel, Chem. Phys. Lett. 183 (1991) 270.

[41] S. Schmidt, T. Arlt, P. Hamm, H. Huber, T. Nägele, J. Wachtveitl, M. Meyer, H. Scheer, W. Zinth, Chem. Phys. Lett. 223 (1994) 116.

[42] N.W. Woodbury, W.W. Parson, Biochim. Biophys. Acta 767 (1984) 345.

[43] J.M. Peloquin, J.C. Williams, X. Lin, R.G. Alden, A.K.W. Taguchi, J.P. Allen, N.W. Woodbury, Biochemistry 33 (1994) 8089.

[44] R.A. Goldstein, L. Takiff, S.G. Boxer, Biochim. Biophys. Acta 934 (1988) 253.

[45] A. Ogrodnik, W. Keupp, M. Volk, G. Aumeier, M.E. Michel-Beyerle, J. Phys. Chem. 98 (1994) 3432.

[46] S.G. Boxer, R.A. Goldstein, D.J. Lockhart, T.R. Middendorf, L. Takiff, J. Phys. Chem. 93 (1989) 8280.

[47] T. Arlt, S. Schmidt, W. Kaiser, C. Lauterwasser, M. Meyer, H. Scheer, W. Zinth, Proc. Natl. Acad. Sci. USA 90 (1993) 11757.

[48] H. Huber, M. Meyer, T. Nägele, I. Hartl, H. Scheer, W. Zinth, J. Wachtveitl, Chem. Phys. 197 (1995) 297.

[49] K. Warncke, P.L. Dutton, Biochemistry 32 (1993) 4769.

[50] M.R. Gunner, P.L. Dutton, J. Am. Chem. Soc. 111 (1989) 3400.

[51] L. Laporte, C. Kirmaier, C.C. Schenck, D. Holten, Chem. Phys. 197 (1995) 225.

[52] L.J. Mancino, D.P. Dean, R.E. Blankenship, Biochim. Biophys. Acta 764 (1984) 46.

[53] A. Labahan, M.L. Paddock, P.H. McPherson, M.Y. Okamura, G. Feher, J. Phys. Chem. 98 (1994) 3417.

[54] R.J. Debus, G. Feher, M.Y. Okamura, Biochemistry 25 (1986) 2276.

[55] N. Liang, J.R. Miller, G.L. Closs, J. Am. Chem. Soc. 111 (1989) 8740.

[56] N. Liang, J.R. Miller, G.L. Closs, J. Am. Chem. Soc. 112 (1990) 5353.

[57] J. Kroon, H. Oevering, J.W. Verhoeven, J.M. Warman, A.M. Oliver, M.N. Paddon-Row, J. Phys. Chem. 97 (1993) 5065.

[58] G. Grampp, W. Jaenicke, J. Chem. Soc. Faraday Trans. 2 81 (1985) 1035.

[59] X. Lin, J.C. Williams, J.P. Allen, P. Mathis, Biochemistry 33 (1994) 13517.

[60] H.L. Axelrod, G. Feher, J.P. Allen, A. Chirino, M. Day, B.T. Hsu, D.C. Rees, Acta Crystallogr. D50 (1994) 596.

[61] R. Huber, Angew. Chem. Int. Ed. Engl. 28 (1989) 848.

[62] N. Adir, H.L. Axelrod, P. Beroza, R.A. Isaacson, S.H. Rongey, M.Y. Okamura, G. Feher, Biochemistry 35 (1996) 2535.

[63] G. Venturolli, A. Mallardi, P. Mathis, Biochemistry 32 (1993) 13245.

[64] J.M. Ortega, P. Mathis, Biochemistry 32 (1993) 1141.

[65] C. Kirmaier, L. Laporte, C.C. Schenck, D. Holten, J. Phys. Chem. 99 (1995) 8903.

[66] A. Ogrodnik, M. Volk, R. Letterer, R. Feick, M.E. Michel-Beyerle, Biochim. Biophys. Acta 936 (1988) 361.

[67] M.R. Gunner, D.E. Robertson, P.L. Dutton, J. Phys. Chem. 90 (1986) 3783.

[68] D. Kleinfeld, M.Y. Okamura, G. Feher, Biochim. Biophys. Acta 766 (1984) 126.

[69] A. Labahan, J.M. Bruce, M.Y. Okamura, G. Feher, Chem. Phys. 197 (1995) 355.

[70] J.J. Hopfield, Proc. Natl. Acad. Sci. USA 71 (1974) 3640.

[71] J. Jortner, J. Chem. Phys. 64 (1976) 4860.

[72] M. Bixon, J. Jortner, M.E. Michel-Beyerle, Chem. Phys. 197 (1995) 389.

[73] S. Franzen, R.F. Goldstein, S.G. Boxer, J. Phys. Chem. 97 (1993) 3040.

[74] D.N. Beratan, J.N. Betts, J.N. Onuchic, Science 252 (1991) 1285.

[75] C.C. Moser, C.C. Page, R. Farid, P.L. Dutton, J. Bioene. Biomemb. 27 (1995) 263.

[76] J. Jortner, J. Am. Chem. Soc. 102 (1980) 6676.

[77] R.A. Marcus, J. Chem. Phys. 24 (1956) 966.

[78] R.A. Marcus, J. Chem. Phys. 26 (1957) 867.

[79] R.A. Marcus, Faraday Discuss. Chem. Soc. 29 (1960) 21.

[80] V.G. Levich, Adv. Electrochem. Electrochem. Eng. 4 (1966) 249.

[81] J. O'M. Bockris, K.L. Mittal, R.K. Sen, Nature Physical Science 234 (1971) 118.

[82] M. Bixon, J. Jortner, J. Phys. Chem. 90 (1986) 3795.

[83] J. Ulstrup, J. Jortner, J. Chem. Phys. 63 (1975) 4358.

[84] N.R. Kestner, J. Logan, J. Jortner, J. Phys. Chem. 78 (1974) 2148.

[85] E. Buhks, M. Bixon, J. Jortner, Chem. Phys. 55 (1981) 41.

[86] M. Bixon, J. Jortner, J. Phys. Chem. 95 (1991) 1941.

[87] M. Bixon, J. Jortner, Chem. Phys. Lett. 159 (1989) 17.

[88] E.W. Knapp, S.F. Fischer, J. Chem. Phys. 87 (1987) 3880.

[89] A. Ogrodnik, N. Remy-Richter, M.E. Michel-Beyerle, R. Feik, Chem. Phys. Lett. 135 (1987) 576.

[90] D. DeVault, Q. Rev. Biophys. 13 (1980) 387.
[91] P.L. Dutton, T. Kihara, J. McCray, J.P. Thornber, Biochim. Biophys. Acta 226 (1971) 81.
[92] B. Hales, Biophys. J. 16 (1976) 471.
[93] M. Bixon, J. Jortner, in J. Jortner, B. Pullman (eds.), Tunneling, Reidel, Dordrecht, 1986, p. 361.
[94] R.A. Marcus, N. Sutin, Biochim. Biophys. Acta 811 (1985) 265.
[95] M. Bixon, J. Jortner, J. Chem. Phys. 89 (1988) 3392.
[96] S.F. Fischer, E.W. Knapp, J. Chem. Phys. 89 (1988) 3394.
[97] B. Cartling, J. Chem. Phys. 95 (1991) 317.
[98] S. Trasatti, Pure Appl. Chem. 58 (1986) 955.
[99] L.I. Krishtalik, Biochim. Biophys. Acta 977 (1989) 200.
[100] M.G. Evans, M. Polanyi, Trans. Faraday Soc. 31 (1935) 875.
[101] L.G. Arnaut, S.J. Formosinho, in M. Chanon (ed.) Homogeneous Photocatalysis, Wiley, New York, 1997, p. 55.
[102] L. Pauling, J. Am. Chem. Soc. 69 (1947) 542.
[103] H.S. Johnston, C.A. Parr, J. Am. Chem. Soc. 85 (1963) 2544.
[104] R.F. Nalewajski, S.J. Formosinho, A.J.C. Varandas, J. Mrozek, Int. J. Quant. Chem. 51 (1994) 187.
[105] N. Agmon, R.D. Levine, Chem. Phys. Lett. 52 (1977) 197.
[106] N. Agmon, Int. J. Chem. Kinet. 13 (1981) 333.
[107] J.C. Light, Disc. Faraday Soc. 44 (1967) 14.
[108] M.R. Fisher, H.J.M. de Groot, J. Rapp, C. Winkel, A.J. Hoff, J. Lugtenburg, Biochem 31 (1992) 11038.
[109] S.J. Formosinho, Tetrahedron 43 (1987) 1116.
[110] S.J. Formosinho, J. Phys. Org. Chem. 3 (1990) 325.
[111] S.J. Formosinho, J. Chem. Soc. Perkin Trans. 2 (1987) 61.
[112] S.J. Formosinho, V.M.S. Gil, J. Chem. Soc. Perkin Trans. 2 (1987) 1655.
[113] S.J. Formosinho, L.G. Arnaut, J. Chem. Soc. Perkin Trans. 2 (1989) 1947.
[114] L.G. Arnaut, S.J. Formosinho, J. Phys. Chem. 92 (1988) 685.
[115] K. Yates, J. Phys. Org. Chem. 2 (1989) 300.
[116] L.G. Arnaut, S.J. Formosinho, J. Phys. Org. Chem. 3 (1990) 95.
[117] L.G. Arnaut, J. Phys. Org. Chem. 4 (1991) 726.
[118] L.G. Arnaut, S.J. Formosinho, J. Photochem. Photobiol. A: Chem. 69 (1992) 41.
[119] L.G. Arnaut, in T. Bountis (ed.), Proton Transfer in Hydrogen-Bonded Systems, Plenum Press, New York, 1992, p. 281.
[120] L.G. Arnaut, S.J. Formosinho, J. Photochem. Photobiol. A: Chem. 75 (1993) 1.
[121] S.J. Formosinho, L.G. Arnaut, J. Photochem. Photobiol. A: Chem. 75 (1993) 21.
[122] W. Gordy, J. Chem. Phys. 14 (1946) 305.
[123] J. Trotter, Acta Crystallogr. 13 (1960) 86.
[124] T. Takano, R.E. Dickerson, J. Mol. Biol. 153 (1981) 95.
[125] T. Takano, R.E. Dickerson, J. Mol. Biol. 153 (1981) 79.
[126] L.O. Peitilä, K. Palmö, B. Mannfors, J. Mol. Spectrosc. 116 (1986) 1.
[127] P. Siders, R.A. Marcus, J. Am. Chem. Soc. 103 (1981) 741.
[128] S.U.M. Khan, J.O.M. Bockris, J. Phys. Chem. 87 (1983) 4012.
[129] K.H. Schmidt, A. Müller, Inorg. Chem. 14 (1975) 2183.
[130] S.U.M. Khan, Z.Y. Zhou, J. Chem. Soc. Faraday Trans. 87 (1991) 535.
[131] I.M. Mills, in A.C.P. Alves, J.M. Brown, J.M. Hollas (eds.), Frontiers of Laser Spectroscopy of Gases, NATO ASI, Kluwer, Dordrecht, 1988, p. 461.
[132] S.J. Formosinho, Mol. Photochem. 7 (1976) 41.
[133] X.-Y. Li, R.S. Czernuszewicz, J.R. Kincaid, Y.O. Su, T.G. Spiro, J. Phys. Chem. 94 (1990) 31.
[134] X.-Y. Li, R.S. Czernuszewicz, J.R. Kincaid, P. Stein, T.G. Spiro, J. Phys. Chem. 94 (1990) 47.
[135] S. Hu, J.R. Kincaid, J. Am. Chem. Soc. 113 (1991) 2843.
[136] S. Hu, J.R. Kincaid, J. Am. Chem. Soc. 113 (1991) 9760.
[137] G.L. Closs, L.T. Calcaterra, N.J. Green, K.W. Penfield, J.R. Miller, J. Phys. Chem. 90 (1986) 3673.
[138] H. Oevering, M.N. Paddon-Row, M. Heppener, A.M. Oliver, E. Cotsaris, J.W. Verhoeven, N.S. Hush, J. Am. Chem. Soc. 109 (1987) 3258.
[139] S.J. Formosinho, L.G. Arnaut, Adv. Photochem. 16 (1991) 67.
[140] R. Englman, A. Ranfani, Physica 98 B (1980) 151.
[141] T. Arai, S. Tobita, H. Shizuka, J. Am. Chem. Soc. 117 (1995) 3968.
[142] R.A. Marcus, J. Chem. Phys. 81 (1984) 4494.
[143] R.A. Marcus, M.E. Coltrin, J. Chem. Phys. 67 (1977) 2609.
[144] H. Frauenfelder, H. Hartmann, M. Karplus, I.D. Kuntz, Jr., J. Kuriyan, F. Parak, G.A. Petsko, D. Ringe, R.F. Tilton, Jr., M.L. Connolly, N. Max, Biochemistry 26 (1987) 254.
[145] R.A. Marcus, Angew. Chem. Int. Ed. Engl. 32 (1993) 1111.
[146] P.F. Barbara, T.J. Meyer, M.A. Ratner, J. Phys. Chem. 100 (1996) 13148.
[147] P. Suppan, Topics Current Chem. 163 (1992) 95.
[148] G. Rauhut, T. Clark, J. Am. Chem. Soc. 115 (1993) 9127.
[149] G. Rauhut, T. Clark, J. Chem. Soc. Faraday Trans. 90 (1994) 1783.
[150] Y. Bu, C. Deng, J. Phys. Chem. A 101 (1997) 1198.
[151] R.M. Nielson, J.T. Hupp, D.I. Yoon, J. Am. Chem. Soc. 117 (1995) 9085.
[152] S.F. Nelsen, D.T. Rumack, M. Meot-Ner (Mautner), J. Am. Chem. Soc. 109 (1987) 1373.
[153] G.E. McManis, R.M. Nielson, A. Gochev, M.J. Weaver, J. Am. Chem. Soc. 111 (1989) 5533.
[154] M.-S. Chan, A.C. Wahl, J. Phys. Chem. 86 (1982) 126.
[155] R.A. Marcus, P. Siddarth, in E. Kochanski (ed.), Photoprocesses in Transition Metal Complexes, Biosystems and Other Molecules. Experiment and Theory, NATO ASI Series, Kluwer, Dordrecht, 1992, p. 49.
[156] T.T.-T. Li, J. Brubaker, C.H. J. Organomet. Chem. 216 (1981) 223.
[157] J. Burgess, E. Pelizzetti, Prog. Reaction Kinetics 17 (1992) 107.
[158] R.M. Nielsen, S. Wherland, Inorg. Chem. 23 (1984) 1338.
[159] N. Hush, Prog. Inorg. Chem. 8 (1967) 391.
[160] J.T. Hupp, Y. Dong, L. Blackbourn, H. J. Phys. Chem. 97 (1993) 3278.
[161] S.F. Nelsen, J. Adamus, J.J. Wolff, J. Am. Chem. Soc. 116 (1994) 1589.
[162] A.K. Churg, R.M. Weiss, A. Warshel, T. Takano, J. Phys. Chem. 87 (1983) 1683.
[163] I. Muegge, P.X. Qi, A.J. Wand, Z.T. Chu, A. Warshel, J. Phys. Chem. B 101 (1997) 825.
[164] G. McLendon, Structure and Bonding 75 (1991) 159.
[165] J. Kroon, J.W. Verhoeven, M.N. Paddon-Row, A.M. Oliver, Angew. Chem. Int. Ed. Engl. 30 (1991) 1358.
[166] G.L. Closs, J.R. Miller, Science 240 (1988) 440.
[167] D. Rehm, A. Weller, Isr. J. Chem. 8 (1970) 259.
[168] T.M. McCleskey, J.R. Winkler, H.B. Gray, J. Am. Chem. Soc. 114 (1992) 6935.
[169] C. Turró, J.M. Zaleski, Y.M. Karabatsos, D.G. Nocera, J. Am. Chem. Soc. 118 (1996) 6060.
[170] J.-M. Chen, T.-I. Ho, C.-Y. Mou, J. Phys. Chem. 94 (1990) 2889.
[171] L.G. Arnaut, S.J. Formosinho, J. Mol. Struct. (Theochem) 233 (1991) 209.
[172] H. Burger, in K.M. Smith (ed.), Porphyrins and Metalloporphyrins, Elsevier, Amsterdam, 1975, p. 525.
[173] J. Burgess, Metal Ions in Solution, Ellis Howard, Chichester, 1978, p. 85.
[174] C.-Y. Lin, T.G. Spiro, J. Phys. Chem. 101 (1997) 472.
[175] D.W. Dixon, X. Hong, S.E. Woehler, A.G. Mauk, B.P. Sishta, J. Am. Chem. Soc. 112 (1990) 1082.
[176] I.R. Gould, S. Farid, Acc. Chem. Res. 29 (1996) 522.
[177] T. Heinis, S. Chowdhury, S.L. Scott, P. Kebarle, J. Am. Chem. Soc. 110 (1988) 400.
[178] T.M. Cotton, R.P. Van Duyne, J. Am. Chem. Soc. 101 (1979) 7605.
[179] G.L. Closs, E.V. Sitzmann, J. Am. Chem. Soc. 103 (1981) 3217.

[180] K. Sasaki, T. Kashimura, M. Ohura, Y. Ohsaki, N. Ohta, J. Electrochem. Soc. 137 (1990) 2437.

[181] T. Layloff, T. Miller, R.N. Adams, H. Fäh, A. Horsfield, W. Proctor, Nature 205 (1965) 382.

[182] Y. Saito, J. Takemoto, B. Hutchinson, K. Nakamoto, Inorg. Chem. 11 (1972) 2003.

[183] H.R. Virdee, R.E. Hester, J. Phys. Chem. 88 (1984) 451.

[184] D.P. Strommen, P.K. Mallick, G.D. Danzer, R.S. Lumpkin, J.R. Kincaid, J. Phys. Chem. 94 (1990) 1357.

[185] M. Mylrajan, L.A. Andersson, J. Sun, T.M. Loehr, C.S. Thomas, E.P. Sullivan, Jr., M.A. Thomson, K.M. Long, O.P. Anderson, S.H. Strauss, Inorg. Chem. 34 (1995) 3953.

[186] M.W. Grinstaff, M.G. Hill, E.R. Birnbaum, W.P. Schaefer, J.A. Labinger, H.B. Gray, Inorg. Chem. 34 (1995) 4896.

[187] D.W. Dixon, M. Barbush, A. Shirazi, J. Am. Chem. Soc. 106 (1984) 4638.

[188] J. Sun, J.F. Wishart, M.B. Gardineer, M.P. Cho, S.S. Isied, Inorg. Chem. 34 (1995) 3301.

[189] D.W. Dixon, X. Hong, S.E. Woehler, Biophys. J. 56 (1989) 339.

[190] R.K. Gupta, Biochim. Biophys. Acta 292 (1973) 291.

[191] J. Breton, E. Nabedryk, W.W. Parson, Biochemistry 31 (1992) 7503.

[192] J.C. Williams, R.G. Alden, H.A. Murchinson, J.M. Peloquim, N.W. Woodbury, J.P. Allen, Biochemistry 31 (1992) 11029.

[193] H.A. Murchinson, R.G. Alden, J.P. Allen, J.M. Peloquim, A.K.W. Taguchi, N.W. Woodbury, J.C. Williams, Biochemistry 32 (1993) 3498.

[194] L. Laporte, L.M. McDowell, C. Kirmaier, C.C. Schenck, D. Holten, Chem. Phys. 176 (1993) 615.

[195] C. Kirmaier, L. Laporte, C.C. Schenck, D. Holten, J. Phys. Chem. 99 (1995) 8910.

[196] N.W. Woodbury, S. Lin, X. Lin, J.M. Peloquin, A.K.W. Taguchi, J.C. Williams, J.P. Allen, Chem. Phys. 197 (1995) 405.

[197] K.M. Giangiacomo, P.L. Dutton, Proc. Natl. Acad. Sci. USA 86 (1989) 2658.

[198] X. Lin, H.A. Murchison, V. Nagarajan, W.W. Parson, J.P. Allen, J.C. Williams, Proc. Natl. Acad. Sci. USA 91 (1994) 10265.

[199] B.A. Heller, D. Holten, C. Kirmaier, Science 269 (1995) 940.

[200] J. Deisenhofer, H. Michel, Angew. Chem. Int. Ed. Engl. 28 (1989) 829.

[201] M.A. Steffen, K. Lao, S.G. Boxer, Science 264 (1994) 810.

[202] P. Mathis, in M. Chanon (ed.), Homogeneous Photocatalysis, Wiley, Chichester, 1997, p. 355.